

Fully microscopic scission-point model to predict fission fragment observables

J.-F. Lemaître* and S. Goriely

Institut d'Astronomie et d'Astrophysique, Université Libre de Bruxelles, Campus de la Plaine CP 226, BE-1050 Brussels, Belgium

S. Hilaire

CEA, DAM, DIF, F-91297, Arpajon, France

J.-L. Sida

CEA, DRF, IRFU, Université Paris-Saclay, F-91191, Gif-sur-Yvette, France

(Received 7 November 2018; revised manuscript received 7 February 2019; published 20 March 2019)

We present an upgraded version of the SPY model, called SPY2 for version 2 of the scission point yield, to estimate mainly the yields and the kinetic energy distributions of fission fragments: The theoretical framework is similar to our previous version, i.e., a statistical scission point model, but this version is based on fully microscopic nuclear ingredients describing the fragments properties at the scission point. These include the static properties of some 7000 nuclei at 120 axial quadrupole deformations, such as binding energies, proton densities, single-particle level schemes, and states densities, coherently calculated within the constrained Hartree-Fock-Bogoliubov model on the basis of the Skyrme BSk27 interaction. The use of microscopic ingredients has been extended to the proton density distribution and the nuclear states densities. Considering realistic proton densities of fragments allows us to improve the definition of the scission point as well as the prediction of the kinetic energy distribution and to link the kinetic energy to the diffuseness of the fragments' proton density. New microscopic nuclear states densities improve the general coherence of the model, in particular regarding the inclusion of the odd-even pairing effect. In this updated SPY2 version, the calculation of the fission yields and kinetic energy distributions is significantly improved and found to be in relatively good agreement with experiments, at least qualitatively. A detailed study is performed for three well known fissioning systems, namely, thermal neutron induced fission of ^{235}U and ^{239}Pu and spontaneous fission of ^{252}Cf . A systematic analysis of the fission mode as well as mean fragments deformation and total kinetic energies has been performed for some 2000 fissioning nuclei with $78 \leq Z \leq 110$ lying between the proton and neutron drip lines.

DOI: [10.1103/PhysRevC.99.034612](https://doi.org/10.1103/PhysRevC.99.034612)**I. INTRODUCTION**

Fission yields represent a key physical quantity of interest in fundamental nuclear physics as well as in many nuclear applications. While in fundamental physics, fission yields provide a direct insight into the probability of fragment formation during the fission process, in nuclear energy applications, they are needed to estimate the accumulation and inventory of fission products at various stages of the nuclear fuel cycle. They also play a key role in nucleosynthesis applications and more specifically in our understanding of the rapid neutron-capture process, or r-process, to explain the origin of about half of the elements heavier than iron in the Universe [1]. The r-process nucleosynthesis in material that is dynamically ejected by tidal and pressure forces during the merging of binary neutron stars is known to be largely insensitive to the detailed astrophysical conditions because of efficient fission recycling [1–3], but remains sensitive to the detailed description of the fission process, including the fission fragment distribution of the heavy neutron-rich nuclei

[2,4]. In particular, the fission yields represent a fundamental input in nucleosynthesis simulations since they define the light species that will be produced by the fission recycling and have been shown to directly imprint the final abundance distribution in the ejected material [2,4].

A renewed statistical scission-point model called scission point yield (SPY) model [5] has been presented in 2015 based on a Wilkins-like definition of the scission point. The goal was to extract all the information that could be defined at the scission point, such as the kinetic energies of the fission fragments, on the basis of state-of-the-art ingredients mainly extracted from microscopic models. The newly microcanonical description of the system, possible by the calculation of the absolute available energies for each fissioning partitions for a given system, allowed us to avoid the use of any free parameter for the thermodynamical description, as compared to the Wilkins *et al.* model. In this first approach, nuclear states densities have been approximated by Fermi-gas distributions and the odd-even effect in masses were washed out since they were not included neither in the individual binding energies of the fission fragments, nor in their states densities. The SPY model has proven its capacity to predict new behaviours like the unexpected asymmetric fission of the light nucleus ^{180}Hg

*jean-francois.lemaitre@ulb.ac.be

found by Andreyev *et al.* [6]. This discovery is consistent with the predicted transition between the symmetric fission of ^{198}Hg and the asymmetric fission of ^{180}Hg [5,7].

We propose to improve here this scission-point model to come as close as possible to a state-of-the-art description for all the ingredients included in the model. First, the scission definition is based now on a microscopic description of proton densities instead of the unrealistic fixed tip-distance used by Wilkins and in the first version of SPY. Second, we use nuclear states densities extracted from the same microscopic model given a global coherence between all the ingredients included in the model. This allows to use individual binding energies with odd-even pairing effects since they are taken into account in all the ingredients. These two major improvements lead us to use the new name of SPY2 to clearly distinguish both versions of the model which are in the same spirit but with different scission definitions and physical ingredients.

For the fission of highly excited nuclei ($Q \gtrsim 100$ MeV), the yields fission are often studied through fusion-fission reactions. In this case, they do not depend on the fragments shell structure since it is washed out at high energies, so that the fissioning nucleus tends to behave as a liquid drop [8]. Denisov *et al.* [9] found that the height of the so-called two-body saddle point is larger than the height of the one-body saddle point (i.e., the fission barrier) for nuclei with $A \lesssim 220$. For heavier nuclei, it is the opposite, so that the yields are expected to be sensitive to the trajectories descending from the one-body saddle point to the scission point. In the low-energy case, i.e., for a few MeV above the fission barrier, fission is better described by an adiabatic process from ground state to saddle point and a statistical one at scission point [10]. In this case, the fragmentations are determined at the last stage of the process with a strong interplay with the fragments properties. At these low energies, the fission of actinides is well known to be asymmetric while several fission modes are found for lighter nuclei. Transition from symmetric to asymmetric fission is observed between proton-rich to neutron-nuclei Th and Pa isotopes [11]. Between symmetric and asymmetric fissioning nuclei, some nuclei (e.g. following the proton-induced fission of ^{226}Ra) also show a triple-hump yields distribution at low energy which corresponds to the superposition of both the symmetric and asymmetric modes [12]. A triple-hump distribution can also appear transiently at medium energy between a double humped asymmetric distribution at low energy and a single humped symmetric distribution at high energy, as found in the neutron-induced fission of ^{232}Th [13]. For other nuclei, the transition of the fission mode with excitation energy goes from asymmetric to symmetric, like in the neutron-induced fission of ^{238}U [14]. A new kind of fission mode, namely a doubly asymmetric fission corresponding to a four humped fission yields distribution, was also predicted by SPY around ^{278}Cf and shown to be crucial to shape the r-abundance distribution around the rare earth peak during the prompt ejecta of neutron star merger [2]. All these complex fission modes need to be understood.

Within the SPY model, fission observables are described based on the nuclear structure properties of the fragments. Fission yields are not the only observables calculated by SPY. Many observables related to fission fragments can be

estimated, such as the kinetic or excitation energies from which the number of evaporated neutrons can be deduced. Thereby, SPY offers a simple coherent framework based only on fragments properties to interpret experimental data and to understand the links between them.

As mentioned in the first version of the SPY model [5], hereafter referred to as SPY1, the initial aim of the model was not to achieve an optimal fit to experimental data for each fissioning system, contrary to the Brosa *et al.* model [15] or the GEF model [16], but rather to describe first qualitatively most fission observables on the basis of the static fission fragment properties at scission. For this reason, fragment properties are described as much as possible on the basis of microscopic models leaving not much space for parameter adjustments. Dynamical effects such as those found in the sophisticated theoretical frameworks of Refs. [17–21] are not taken into account in the present study.

After a general theoretical reminder, the updated version of the SPY model is presented in Sec. II together with its various microscopic ingredients in Sec. III. In Sec. IV, the results for the three well-known fissioning nuclei ^{236}U , ^{240}Pu , and ^{252}Cf are discussed in details and compared with available experimental data, before presenting the SPY2 predictions for all bound nuclei beyond platinum in Sec. V. Conclusions are drawn in Sec. VI.

II. SPY MODEL

The SPY model is a static and statistical scission-point model [22] that assumes a thermodynamic equilibrium at scission, hence neglecting the evolution between the saddle and the scission points. The model is based on two pillars, namely, the absolute available energy balance at the scission configuration and the statistical description of the phase space available.

The available energy balance is performed for all energetically possible fragmentations of a fissioning system at scission (around 1000 for actinide fission) as a function of the deformation parameter \tilde{q} of both fragments. The available energy,

$$E_{\text{avail}} = E_{\text{ind}}(Z_1, N_1, \tilde{q}_1) + E_{\text{ind}}(Z_2, N_2, \tilde{q}_2) + E_{\text{coul}}(Z_1, N_1, \tilde{q}_1, Z_2, N_2, \tilde{q}_2) + E_{\text{nucl}}(Z_1, N_1, \tilde{q}_1, Z_2, N_2, \tilde{q}_2) - E_{\text{CN}}^*, \quad (1)$$

is defined as the difference between the potential energy of the fissioning system at scission and the energy ($E_{\text{CN}}^* = E_{\text{CN}} + Q$) of the excited compound nucleus where both nascent fragments are supposed to be at rest. The potential energy of the fissioning system at scission is obtained as the sum of the individual binding energies of the two fragments (E_{ind}) and the interaction energy between the fragments composed of the Coulomb repulsion (E_{coul}) and the nuclear attraction (E_{nucl}). A fragmentation is energetically possible only if $E_{\text{avail}} < 0$. For convenience, the absolute value of the available energy is used hereafter, i.e., only energetically possible fragmentations are taken into account.

The system at scission is treated as a microcanonical ensemble where all available states are equiprobable. In this

framework, the number of available states of a given fragmentation (π) is the product of the state densities (ρ) of the two isolated fragments and can be expressed as

$$\begin{aligned} \pi(Z_1, N_1, \tilde{q}_2, Z_2, N_2, \tilde{q}_2, x) \\ = \rho_1[xE_{\text{avail}}]\rho_2[(1-x)E_{\text{avail}}]\delta E^2, \end{aligned} \quad (2)$$

where a fraction x of the available energy goes to fragment 1 and the remaining fraction $(1-x)$ goes to fragment 2. For a given observable \mathcal{O} of a fragment (Z, N), its mean value $\langle \mathcal{O} \rangle$ is estimated by

$$\langle \mathcal{O} \rangle = \iint_{\tilde{q}_1, \tilde{q}_2} \int_0^1 \mathcal{O} \pi dx d\tilde{q}_1 d\tilde{q}_2. \quad (3)$$

The two main fission observables studied in the present paper (Sec. IV) are the fission yields (Y) and the kinetic energy (KE).

III. NUCLEAR INPUTS TO THE SPY MODEL

A. Individual binding energies

One fundamental ingredient in the SPY model is the individual binding energy of each fission fragment as a function of its axial deformation. This quantity is estimated within the framework of the constrained self-consistent Hartree-Fock-Bogoliubov (HFB) formalism using the Skyrme BSk27 effective nucleon-nucleon interaction [23] for about 7000 nuclei from $Z = 20$ to $Z = 100$. The BSk27 Skyrme force has been shown to predict all the 2353 experimental masses with an unprecedented root-mean-square deviation of only 0.5 MeV. At the same time, the BSk27 Skyrme functional yields a realistic description of infinite homogeneous nuclear matter properties, as determined by realistic calculations and by experiments; these include in particular the incompressibility coefficient, the pressure in charge-symmetric nuclear matter, the neutron-proton effective mass splitting, the stability against spin and spin-isospin fluctuations, as well as the neutron-matter equation of state.

Constrained HFB wave functions $|\Psi(Q_{20})\rangle$ are obtained by minimizing a Routhian,

$$E = \langle \Psi | \hat{H} - \lambda_N \hat{N} - \lambda_Z \hat{Z} - \sum_i \lambda_i \hat{Q}_{i0} | \Psi \rangle, \quad (4)$$

where $|\Psi\rangle = |\Psi(Q_{20})\rangle$ and $Q_{20} = \langle \Psi | \hat{Q}_{20} | \Psi \rangle$. In the following, the quadrupole moment (Q_{20}) is replaced by the so-called reduced quadrupole moment (\tilde{q}) defined as

$$\tilde{q} = \frac{Q_{20}}{AR_0^2}, \quad (5)$$

where A is the nuclear mass and R_0 its radius ($R_0 = 1.2A^{1/3}$). Constrained HFB calculations are performed for some 120 axial quadrupole deformations within the $\tilde{q} = -0.4$ to $\tilde{q} = 1.6$ range, which is slightly wider than the one used in our former version SPY1, the upper deformation being increased from 1.1 to 1.6 to explore all possible deformations even if the available energy becomes negligible.

While in SPY1, the odd-even staggering was washed out in individual binding energies and not included in state densities

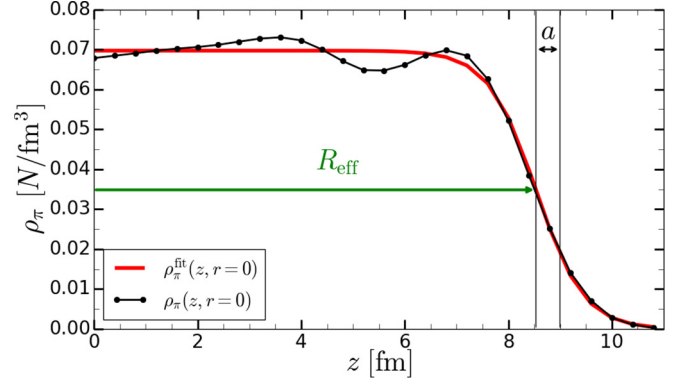


FIG. 1. Fit of axial proton density $\rho_\pi(r, z = 0)$ of ^{104}Mo with $\tilde{q} = 0.91$.

[5,7], it is now included consistently in both descriptions for the SPY2 version.

B. New scission-point definition

The scission point is now defined on the basis of the proton density of the fissioning nucleus using microscopic proton spatial distribution from HFB calculations. This new definition does not consider the nucleon density since the deformation of the fissioning nucleus at the last stage of the fission process, i.e., just before splitting apart, is essentially driven by the Coulomb repulsion, the nuclear attraction becoming negligible to bind protons together [17]. The Coulomb repulsion leads to the splitting of the proton distribution of the fissioning nucleus into two separate distributions. The proton density at the scission neck is now used as a separation criterion for the nascent fragments. The spatial proton distribution of a given nucleus at a given deformation is denoted by $\rho_\pi(z, r)$ and depends only on the axial z and radial r coordinates due to our assumption of an axial symmetry.

We assume here that the scission occurs when the proton density at scission is equal to $\rho_\pi^{\text{neck}} = 0.002 \text{ fm}^{-3}$, so that the external radius of each fragment R_{ext} is such that its axial proton density is half the neck density, i.e.,

$$\rho_\pi(z = R_{\text{ext}}, r = 0) = 0.5 \rho_\pi^{\text{neck}} = 0.001 \text{ fm}^{-3}. \quad (6)$$

This value is kept constant for all nuclei in the present study. It can be considered as a free parameter playing the same role as the scission distance d in SPY1 [5]. A sensitivity analysis with respect to ρ_π^{neck} will be performed in Sec. IV D.

To avoid numerical uncertainties, the HFB axial proton density is fitted by the Fermi function

$$\rho_\pi(z) = \frac{\rho_0}{1 + e^{(z - R_{\text{eff}})/a}}, \quad (7)$$

where ρ_0 is the central (proton) density, R_{eff} is the effective (proton) radius, i.e., $\rho_\pi(z = R_{\text{eff}}, r = 0) = \rho_0/2$ and a is the diffuseness corresponding to the distance over which the axial proton density drops from $0.5\rho_0$ for $z = R_{\text{eff}}$ to $\rho_0/(1+e) \approx 0.27\rho_0$ for $z = R_{\text{eff}} + a$ (Fig. 1).

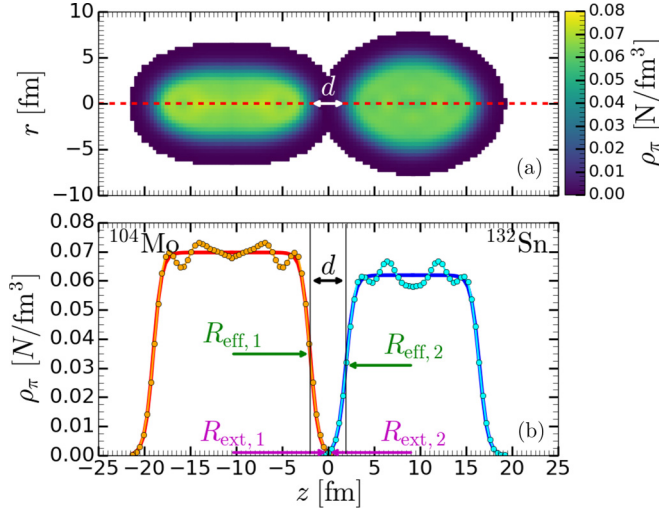


FIG. 2. (a) Color-coded proton density distribution for the scission configuration of ^{236}U into $^{104}\text{Mo}(\bar{q} = 0.91) + ^{132}\text{Sn}(\bar{q} = 0.3)$ in the (z, r) plane. (b) Axial proton density (dot symbols) and fitted axial densities (solid line) for the same system as in (a). The scission distance d is deduced from external and effective radii as shown on both panel. The red dashed line in the top panel (a) represents the scission axis and its corresponding proton density (axial proton density) is displayed in the bottom panel (b).

With a Fermi function, the external radius is well determined as

$$R_{\text{ext}} = a \ln \left(\frac{\rho_0}{0.5\rho_{\pi}^{\text{neck}}} - 1 \right) + R_{\text{eff}}. \quad (8)$$

Fragments are located on the same symmetry axis and the distance between the centers of each proton distribution is given by $R_{\text{ext},1} + R_{\text{ext},2}$. The resulting proton distributions are illustrated in Fig. 2 for the ^{236}U fragmentation into $^{104}\text{Mo}(\bar{q} = 0.91) + ^{132}\text{Sn}(\bar{q} = 0.3)$.

A scission distance can be deduced from the scission configuration [Fig. 2(b)]. Clearly, such a distance varies with the fissioning system and therefore differs with respect to distance used in the SPY1 version where a constant value of $d = 5$ fm was imposed. Now, the scission distance

$$d = R_{\text{ext},1} - R_{\text{eff},1} + R_{\text{ext},2} - R_{\text{eff},2} \quad (9)$$

is defined from the external and effective fragment radii. The scission distance, correlated to the neck density, is generally smaller than 5 fm irrespective of the fragmentation and varies significantly with the fragments deformation (\bar{q}_1, \bar{q}_2) . As an example, for the ^{236}U fragmentation into $^{104}\text{Mo} + ^{132}\text{Sn}$, d varies from 3 fm for large deformations to 4 fm for medium deformations, as shown in Fig. 3. This new definition of the scission point also introduces a diffuseness dependence in the Coulomb energy, as discussed in Sec. IV C.

C. Coulomb interaction energy

In SPY1, the proton distributions of both fragments were assumed to be uniform, without diffuseness. The shape was parametrized by an axial quadrupole deformation using Legend polynomials and the Coulomb interaction energy was

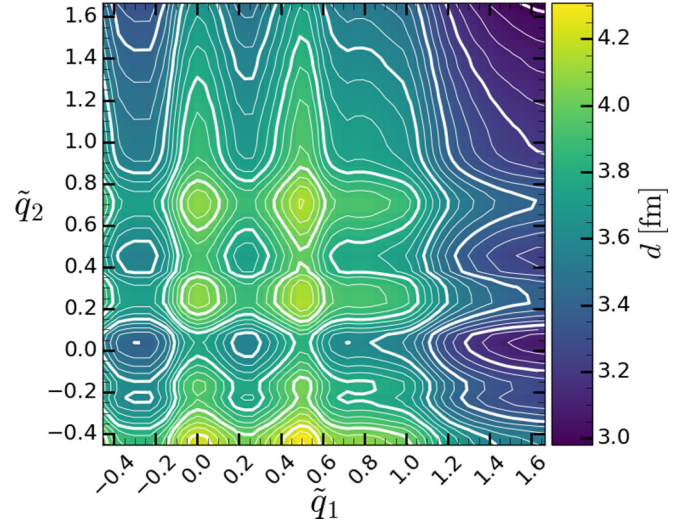


FIG. 3. Scission distance for the ^{236}U fragmentation into $^{104}\text{Mo} + ^{132}\text{Sn}$ depending on their deformation parameters \bar{q}_1 and \bar{q}_2 .

computed by numerical folding using a specific integration mesh [5]. For SPY2, an improved technique has been developed to compute the Coulomb interaction energy between the proton distributions of both fragments at scission, as illustrated in Fig. 2(a). A trivial way to compute the Coulomb energy is to integrate over $x, y,$ and z coordinates of both fragments. From a numerical point of view, this procedure would imply six nested loops which would be extremely time consuming.

Due to the axial symmetry of the fragments, their proton distribution corresponds to a set of coaxial hollow cylinders nested on each other with a variable proton density. The outer hollow cylinders have a proton density close to zero whereas the inner ones have a high proton density. The Coulomb interaction energy is the sum of the interactions between the two sets of hollow cylinders which is translated from a computational point of view into four nested loops. Each configuration of two coaxial hollow cylinders are characterized by the shape parameters α and β plus the shape factor $g(\beta)$ which depend on the radius r , thickness Δr and width Δz of the cylinders as well as the distance between them. The computation time is lowered by precomputing the shape factor $g(\beta)$ for many values of β between 0 and 1. The use of shape factors is possible thanks to the axial symmetry of the fissioning system at scission (more details can be found in Appendix A).

The Coulomb energy surface for a given fragmentation is less smooth with our new HFB proton densities [Fig. 4(b)] than they used to be with uniform profiles as in SPY1 [Fig. 4(a)]. This feature is mainly due to the variable scission distance introduced by the new scission definition (Fig. 3) and related to the diffuseness of the fragment proton densities.

D. Nuclear interaction energy

The nuclear interaction energy is estimated on the basis of the Blocki proximity potential [24]

$$E_{\text{nucl}} = 4\pi\gamma(I)\bar{R}b\Phi(d/b), \quad (10)$$

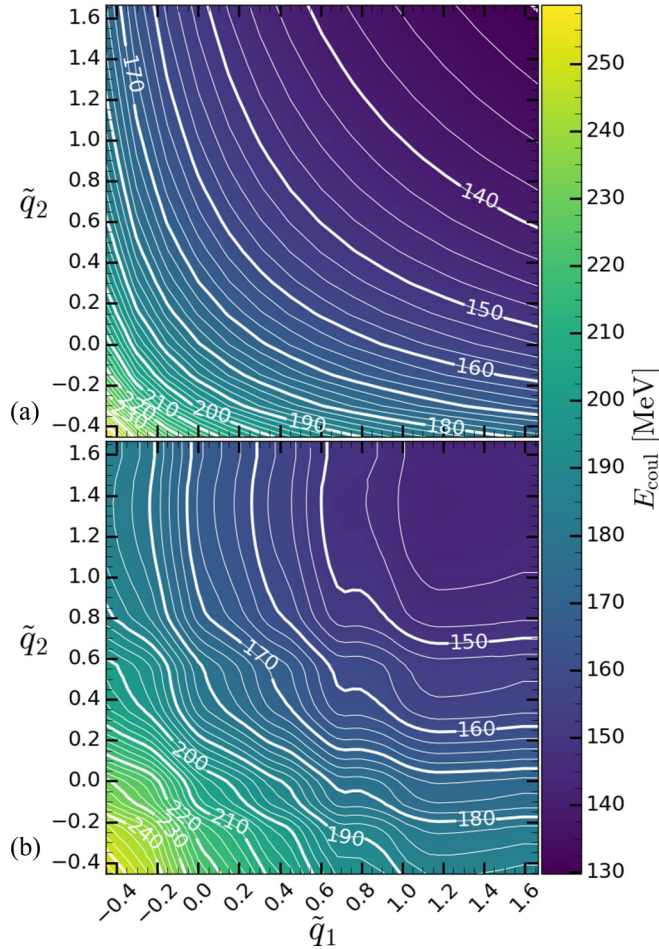


FIG. 4. Coulomb interaction energy for the ^{236}U fragmentation into $^{104}\text{Mo} + ^{132}\text{Sn}$ as a function of their deformation parameters \tilde{q}_1 and \tilde{q}_2 . Top panel (a) is computed with uniform proton densities and $d = 5$ fm (corresponding to SPY1). Bottom panel (b) is computed with HFB-fitted proton distributions and our new scission-point definition as detailed in the text.

which depends on the scission distance d , the surface width $b = 1$ fm, the isospin asymmetry $I = (N - Z)/A$ of the fissioning system, the reduced radii of curvature \bar{R} :

$$\frac{1}{\bar{R}} = \frac{1}{R_1} + \frac{1}{R_2}, \quad (11)$$

which is the geometric mean of the main deformation-dependent radii of curvature of both fragments $R_i(\tilde{q}_i)$ at their nearest points and the surface energy coefficient $\gamma(I) = 0.9517(1 - 1.7826I^2)$ [MeV/fm²]. The ‘‘cubic-exponential’’ pocket formula $\Phi(d/b)$ is used as a dimensionless proximity potential function. More details can be found in Ref. [24].

Thanks to the analytical expression of the nuclear interaction energy Eq. (10) its computation time remains low. As illustrated in Fig. 5(a) for the ^{236}U fragmentation into $^{104}\text{Mo} + ^{132}\text{Sn}$, the nuclear energy depends on the scission distance. The highest scission distance is obtained for medium deformations ($0 < \tilde{q} < 0.8$) (Fig. 3), which leads to a nuclear energy close to zero.

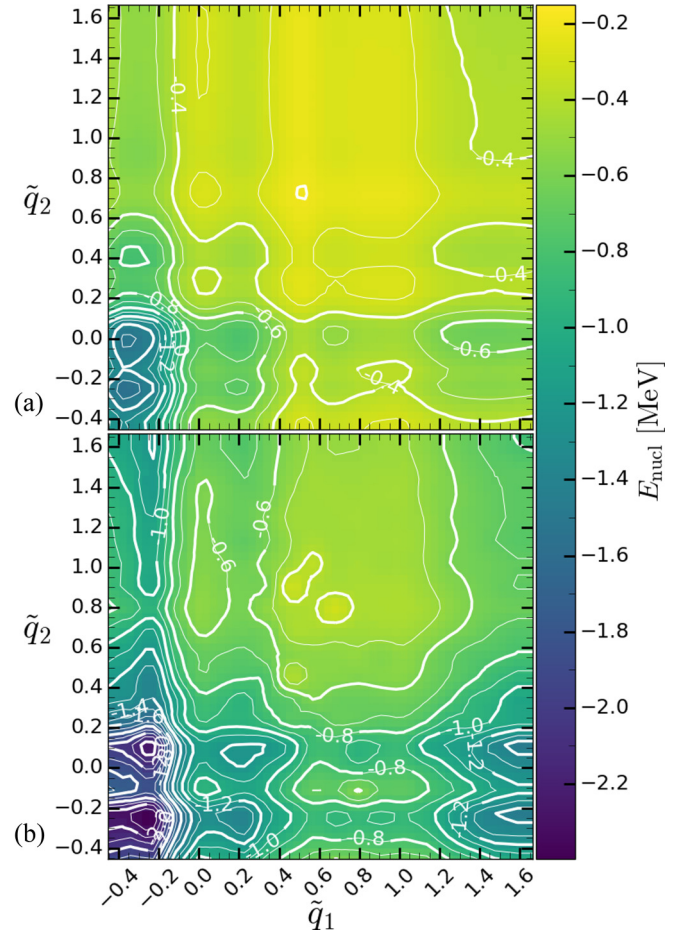


FIG. 5. Nuclear interaction energy for the ^{236}U fragmentation into $^{104}\text{Mo} + ^{132}\text{Sn}$ depending on their deformation parameters \tilde{q}_1 and \tilde{q}_2 . (a) Computed with Blocki proximity potential. (b) Computed with nucleon distributions.

To validate this approximation, the nuclear interaction energy is also computed using detailed HFB nucleon distribution [Fig. 5(b)]. The way to calculate it is similar to the one used for Coulomb interaction energy, although the shape factors $\tilde{f}(\beta, R_k)$ differ in this case; see Appendix B for more details. The deformation dependence of the nuclear energy computed using the nucleon distributions is seen in Fig. 5 to be rather similar to the one computed with the Blocki proximity potential and both predictions remain rather similar within a few 0.1 MeV. Because of the low contribution stemming from the nuclear interaction, the Blocki proximity potential appears to be a satisfactory approximation that we adopt in the present study. The nuclear interaction is seen to have no impact on the fission yields, as illustrated in Fig. 6(a) and 6(b) in the case of the fission of ^{240}Pu ($Q = 6.5$ MeV), when the neck density criteria remains low. The various nuclear interaction energies differ by less than 1 MeV for a neck density of 0.002 or 0.004 fm⁻³ [Figs. 6(d) and 6(e)]. This is due to the large distance between fragments: $\langle d \rangle = 3.91$ fm for $\rho_\pi^{\text{neck}} = 0.002$ fm⁻³ and $\langle d \rangle = 3.20$ fm for $\rho_\pi^{\text{neck}} = 0.004$ fm⁻³. However, choosing higher proton densities at the scission neck, fragments get closer to each other and a more accurate

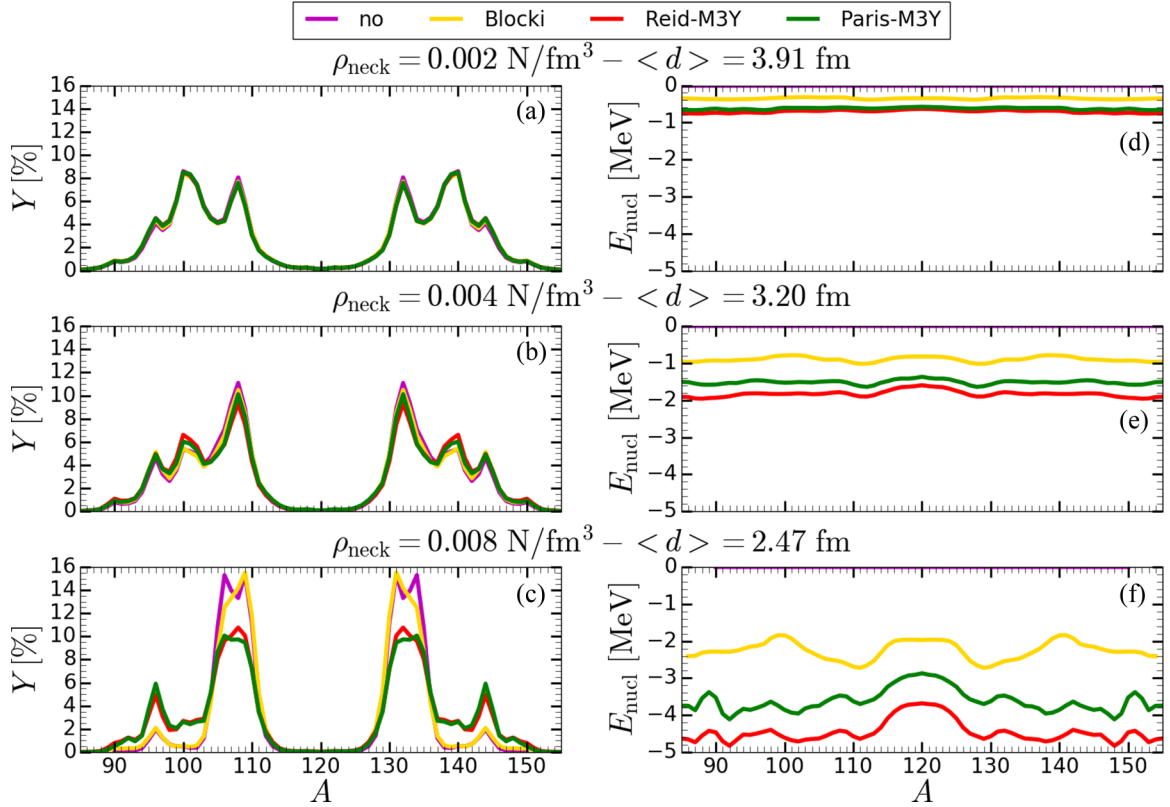


FIG. 6. Left panels (a–c), fission yields of ^{240}Pu ($Q = 6.5$ MeV) for four different estimates of the nuclear interaction energy and three proton densities at scission neck, namely $\rho_{\pi}^{\text{neck}} = 0.002$ (a), 0.004 (b), and 0.008 fm^{-3} (c). The purple line, denoted as “no,” neglects the nuclear interaction energy; the yellow solid line corresponds to the Blocki approximation [24]; while the red and green solid lines are obtained with the Reid-M3Y [25,26] or Paris-M3Y [26] effective nucleon-nucleon interaction, respectively. Right panels (d–f), corresponding nuclear interaction energies.

calculation of the nuclear interaction may be needed. For such proton density at scission neck, the Blocki proximity potential remains valid from the fission yields distribution point of view and has a negligible impact on the KE distribution. However for higher densities, like the $\rho_{\pi}^{\text{neck}} = 0.008$ fm^{-3} case [Figs. 6(c) and 6(f)], the fragments get so close to each other, with a mean distance $\langle d \rangle$ around 2.47 fm, that the adopted model for calculating the nuclear interaction energy impacts the fission yields [Fig. 6(c)]. The Blocki nuclear energy is around -2 MeV regardless of the fragmentations, whereas a value of -4 MeV is obtained with the more complete estimate based on the HFB nucleon distributions [Fig. 6(f)]. The impact of ρ_{π}^{neck} on fission yields, KE and mean deformations will be further discussed in Sec. IV D.

E. Nuclear state density

In SPY1, the Fermi gas state density [27] for a two-fermion system,

$$\rho(U) = \frac{\sqrt{\pi}}{12} \frac{e^{2\sqrt{\tilde{a}U}}}{\tilde{a}^{1/4}U^{5/4}}, \quad (12)$$

was considered with the two-components (proton and neutron) level density parameter \tilde{a} . However, such a simple formulation does not take any pairing or shell effects into account. Similarly, deformation effects are included empirically

for ground state deformation by increasing the \tilde{a} -parameter from $A/13$ to $A/8$, but otherwise Eq. (12) remains deformation independent.

To take pairing, shell, and deformation effects coherently into account, the nuclear state density of a given nucleus at a given deformation is now calculated in the framework of the statistical model of nuclear level densities [28–31] on the basis of the discrete single-particle level scheme, consistently determined within the constrained HFB calculations previously introduced (Sec. III A). Starting from BSk27 [23] proton and neutron HFB single-particle level schemes $\{\varepsilon_q^k\}$ (where $q = n$ or p refers to proton or neutron, respectively, and k refers to the k -th level of the scheme), the chemical potential λ_q and the pairing gap Δ_q are calculated by solving BCS equations within the constant- G approximation [31], namely,

$$N_q = \sum_k 1 - \frac{\varepsilon_q^k - \lambda_q}{E_q^k} \tanh\left(\frac{E_q^k}{2T}\right), \quad (13)$$

$$\frac{2}{G_q} = \sum_k \frac{1}{E_q^k} \tanh\left(\frac{E_q^k}{2T}\right), \quad (14)$$

where $E_q^k = \sqrt{(\varepsilon_q^k - \lambda_q)^2 + \Delta_q^2}$ is the quasiparticle energy, T is the nuclear temperature, and all single-particle states ε_q^k up to 40 MeV in the continuum are included in the summation.

The pairing strength G_q is extracted from the pairing gap equation at zero temperature [Eq. (14)]. In turn, the pairing gap at zero temperature Δ_q^0 is estimated by the five-points approximation [32],

$$\Delta_{0,q} = \frac{1}{8} |M(N_q + 2) - 4M(N_q + 1) + 6M(N_q) - 4M(N_q - 1) + M(N_q - 2)|, \quad (15)$$

where $M(N_q)$ is the nuclear mass and $N_q = Z$ or N . The pairing gap is assumed to be deformation independent; the choice of such an approximation and its impact on the yields will be discussed in Sec. IV B.

Using the chemical potential λ_q and the pairing gap Δ_q , the energy E , entropy S , and total excitation energy U are estimated

$$E(T) = \sum_{q=n,p} \sum_k \varepsilon_q^k \left[1 - \frac{\varepsilon_q^k - \lambda_q}{E_q^k} \tanh \left(\frac{E_q^k}{2T} \right) \right] - \frac{\Delta_q^2}{G_q}, \quad (16)$$

$$S(T) = 2 \sum_{q=n,p} \sum_k \ln(1 + e^{-E_q^k/T}) + \frac{E_q^k/T}{1 + e^{E_q^k/T}}, \quad (17)$$

$$U(T) = E(T) - E(T=0). \quad (18)$$

Finally, the state density is determined by the partition function method with a correction at asymptotic limit to avoid the unphysical divergence at zero temperature [31],

$$\frac{1}{\omega(U)} = (2\pi)^{3/2} \left[\frac{\sqrt{D(U)}}{e^{S(U)}} + \frac{1}{\omega_0(U)} \right], \quad (19)$$

$$\omega_0(U) = \frac{\pi^2 e}{12 T \sqrt{S_n(U) S_p(U)}} e^{S_n(U) S_p(U)}, \quad (20)$$

where $S(U) = S_n(U) + S_p(U)$ is the total entropy of the nucleus and $D(U)$ is the determinant of the second derivatives of the grand partition function [28].

This formalism is known to lead to discontinuities in the state density [29] due to the transition between the superconducting and normal phases of neutrons and protons [Fig. 7(b)]. The level density parameter (a_{1c}) shown in Fig. 7(b) corresponds to the one-component equivalent a -parameter deduced from the Fermi gas state density for a one-fermion system [27],

$$\rho(U) = \frac{1}{\sqrt{48}} \frac{e^{2\sqrt{a_{1c}U}}}{U}. \quad (21)$$

Note that the level density parameter is preferred to the state density to illustrate the nuclear structure evolution with excitation energy. In the example of the ^{104}Mo state density at the deformation $\tilde{q} = 0.09$ [Fig. 7(b)], the level density parameter tends to an asymptotic value at increasing temperature corresponding to a total disappearance of the nuclear structure effects at large excitation energies.

In the BCS theory, the pairing gap fluctuations are neglected which leads to the gap equation [Eq. (14)]. It predicts the existence of a critical temperature at which the pairing gap vanishes, hence a discontinuity appears [29] for quantities depending on the derivative of the pairing gap like the

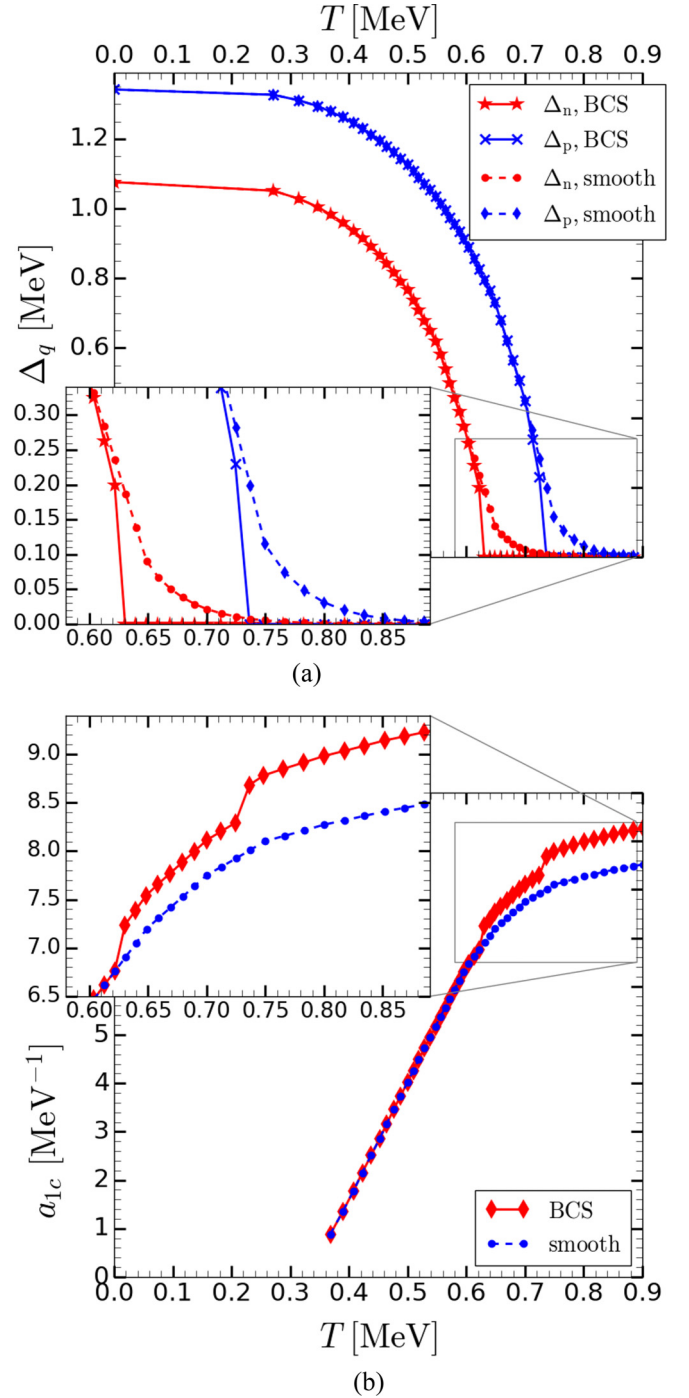


FIG. 7. (a) Pairing gap and (b) one-component level density parameter a_{1c} evolution with temperature for ^{104}Mo at the deformation $\tilde{q} = 0.09$. The insert shows the difference between the BCS (solid line) and smoothed (dashed line) pairing gap around critical temperatures.

determinant $D(U)$ or the heat capacity. The nucleus contains two types of fermions, neutrons and protons, hence there are two critical temperatures leading to two discontinuities. Such discontinuities, characteristic of a second order transition, are unphysical since fluctuations tend to smooth out such sharp phase transitions [33]. More specifically, the discontinuities in

the a parameter stem from the singularity in the determinant calculation, more precisely from K and KL values in Eq. 20 of Ref. [28], i.e.,

$$K_q = \beta \Delta_q \frac{\partial \Delta_q}{\partial \beta}, \quad (22)$$

$$K_q L_q = \beta \Delta_q \frac{\partial \Delta_q}{\partial \mu_q}, \quad (23)$$

where $\beta = 1/T$ and $\mu_q = \beta \lambda_q$. These discontinuities occur at the neutron and proton critical temperatures $T_{q,c}$, when K_q and $K_q L_q$ are equal to zero for $T \geq T_{q,c}$. For ^{104}Mo at the deformation $\tilde{q} = 0.09$ (Fig. 7), these discontinuities occur at $T_{c,n} = 0.63$ MeV and $T_{c,p} = 0.74$ MeV which correspond to the drop of Δ_q from the supraconducting to the normal phase [Fig. 7(a), solid lines].

To avoid such discontinuities, pairing gaps are smoothed around their critical temperatures to lift singularities of K_q and $K_q L_q$ at these temperatures [Fig. 7(a), dashed lines]. The prescription to smooth them is inspired from Ref. [33] and consists in fitting the BCS pairing gaps $\Delta_q(T)$ by the simple expression

$$\Delta_{\text{fit}}(T) = \frac{\Delta_m}{1 + \exp\left[\frac{T - T_m}{T_m} \ln\left(\frac{\Delta_q^0}{\Delta_m - \Delta_q^0}\right)\right]}. \quad (24)$$

Such a prescription suppresses discontinuities in the state density [Fig. 7(b), dashed line] and has been applied systematically in the determination of state densities at all deformations.

IV. RESULTS FOR SOME FISSIONING SYSTEMS

In this section, experimental data are always represented in black solid line with dots. The preneutron isobaric fission yields of three well-known fissioning systems are studied. The first two cases correspond to the thermal neutron-induced fission of ^{235}U and ^{239}Pu where the experimental data are, respectively, from Romano *et al.* [34] and Tsuchiya *et al.* [35]. To compare predictions from SPY1 and SPY2 with experimental data, we take into account an excitation energy of $Q = 6.5$ MeV in the ^{236}U and ^{240}Pu compound nucleus. The last case is the spontaneous fission of ^{252}Cf , where the experimental data are from Zeynalov *et al.* [36], which is compared to SPY data without excitation energy ($Q = 0$ MeV). The other most experimentally accessible fission observable, i.e., the total kinetic energy (TKE) and the kinetic energy per fragment (KE) distributions, are also compared with SPY1 and SPY2 predictions. The TKE is defined as the mean value of Coulomb plus nuclear interaction energy between fragments and the KE is the TKE component carried by a fragment and is deduced from the TKE using the total momentum conservation,

$$\text{KE} = \frac{A_{\text{CN}} - A}{A_{\text{CN}}} \text{TKE}. \quad (25)$$

The experimental KE distribution for the three fissioning system are, respectively, from Baba *et al.* [37], Nishio *et al.* [38], and Hamsch *et al.* [39]. Since this model focuses on the scission-point description, the neutron evaporation of the

fission fragments is not included in the yields distribution, i.e., our predictions are compared with experimental data before neutron emission.

A. Fission yields and Kinetic energy

We compare in Fig. 8 the experimental yields and KE distributions of the three fissioning systems ^{236}U , ^{240}Pu , and ^{252}Cf with those predicted by SPY1 and SPY2. With SPY1 [Figs. 8(a)–8(c), blue dashed lines], the yields distribution are peaked around $A_1 = 132$ and $A_2 = A_{\text{CN}} - 132$ (where A_2 is the second complementary fragment), particularly for U and Pu. These peaked distributions can be explained by the high sensitivity to the fragments shell effect, in particular to the doubly magic nucleus $^{132}_{50}\text{Sn}_{82}$ which is associated with the soft fragment $^{104}_{42}\text{Mo}_{62}$ in the ^{236}U case. Compared to SPY1, the SPY2 yields distributions [Figs. 8(a)–8(c), green thin lines] are much wider and also closer to experimental data but present strong staggering patterns. To compare the overall structure of the yields distribution with experimental data, the distributions are smoothed by a normalized Gaussian function,

$$Y_{\text{smooth}}(Z, N) = \sum_{i,j=-4}^4 Y_{\text{raw}}(Z+i, N+j) C^2 e^{-\frac{i^2+j^2}{2\sigma_{z,n}^2}}, \quad (26)$$

where C is the normalization factor and $\sigma_{z,n} = 0.65$. The choice of this value as well as the impact of this smoothing procedure on the isotopic yields will be discussed in Sec. IV F. Results after smoothing are shown by red lines in Fig. 8.

In the U case [Fig. 8(a), red line], the symmetric part of the distribution is overestimated compared to experimental data. This is partially due to an underestimate of the highly asymmetric part of the yields distribution, which, in turn, is due to an overestimate of the KE for asymmetric fragments [Fig. 8(d), red line]. A lower KE of these asymmetric fragments would increase their available energy, hence their probability, and consequently decrease the symmetric contribution.

The SPY2 Pu yields distribution [Fig. 8(b), red line] matches fairly well the experimental one. Like in the U case, yields of the high asymmetric fragmentations are underestimated due to an overestimate of the KE of the highly asymmetric fragmentations [Fig. 8(e), red line].

In the Cf case [Fig. 8(c)], the peak around $A = 132$ completely disappears with respect to SPY1. The slightly asymmetric yields are underestimated due to an overestimate of the peaks height, i.e., an underestimate of the KE [Fig. 8(f)] for these slightly asymmetric fragments.

Concerning the KE distributions [Figs. 8(d)–8(f)], apart from an overestimate of the KE for the highly asymmetric fragmentations, the HFB proton distributions improve significantly the KE distribution with respect to the uniform sharp proton distributions considered in SPY1. Fission yields and KE distributions are linked via the available energy balance. An overestimate of the KE leads to an underestimate of yields.

In this new version of the SPY model, the yields distributions are more structured due to the inclusion of pairing in individual binding energies and in state densities. Compared

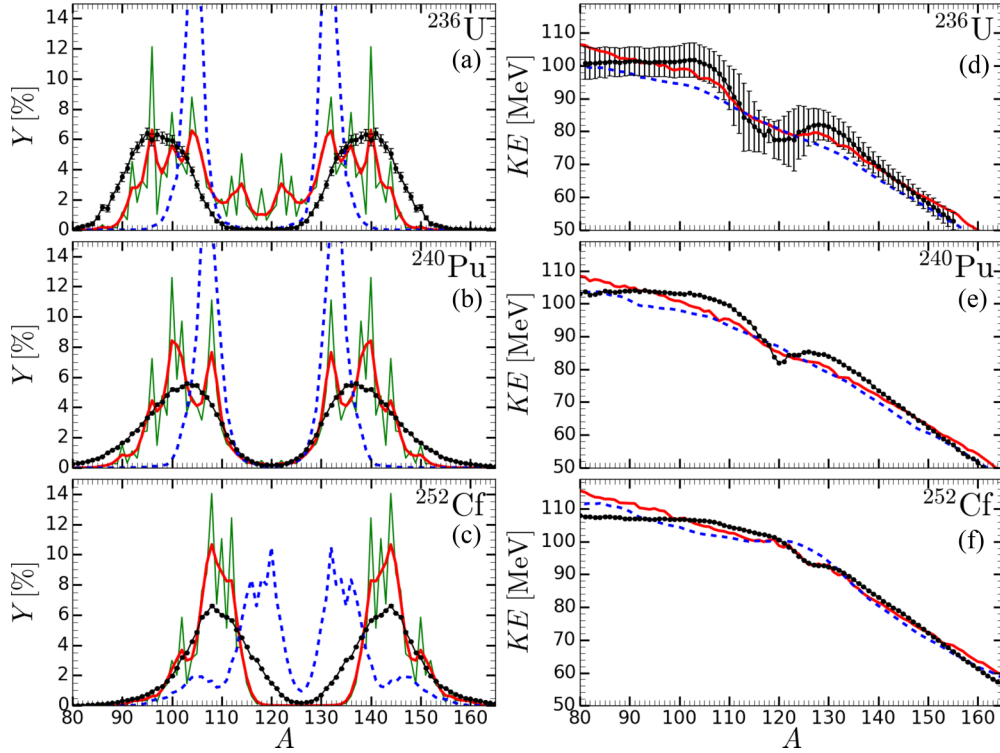


FIG. 8. On the left panels, the black dotted lines represent experimental (pre-neutron-emission) fission yields for fission of ^{236}U ($Q = 6.5$ MeV) (a) [34], ^{240}Pu ($Q = 6.5$ MeV) (b) [35], and fission of ^{252}Cf (c) ($Q = 0$ MeV) [36]. The green thin lines are raw fission yields and the red lines are smooth yields both from SPY2. The blue dashed lines represent experimental KE distribution for fission of ^{236}U ($Q = 6.5$ MeV) (d) [37] and ^{240}Pu ($Q = 6.5$ MeV) (e) [38], and fission of ^{252}Cf ($Q = 0$ MeV) (f) [39]. The red lines are KE distribution from SPY2 and the blue dashed one from SPY1.

to experimental data, the odd-even effect seems slightly too strong [Figs. 8(a)–8(c), green curves] but it is not detrimental to the location and width of the peaks in the yields distribution. The width increase in the fission yields is due to the competition between the shell effects in individual binding energies and those in state densities; the shell effects have antagonist effects on available energy and available states. The pairing correlations reduce the intrinsic energy of the even-even nuclei, hence increases the available energy for the corresponding fragmentations. At the same time, these correlations decrease the state density and the number of available states. These two effects tend to cancel each other to some extent. Shell effects have a similar impact, but with a larger amplitude, especially for closed-shell nuclei. Fragmentations with shell closures are not necessarily the most probable configuration with SPY2, in contrast to SPY1 predictions. The impact of shell effects will be further detailed in Sec. V.

B. Impact of the pairing gap on the fission yields

As described in Sec. III E, the pairing strength affecting nuclear state densities has been determined on the basis of the five-points mass difference [Eq. (15)]. To test the sensitivity of our results to this approximation, we also considered the deformation-dependent pairing strength G_q extracted from the

HFB pairing energy at a given nuclear deformation, i.e.,

$$E_{p,q}^{\text{HFB}} = -\frac{\Delta_{0,q}^2}{G_q} = -\frac{\Delta_{0,q}^2}{2} \sum_k \frac{1}{E_q^k}. \quad (27)$$

The HFB pairing energy has been estimated within an energy range of $\varepsilon_\Lambda = 16$ MeV around the Fermi energy ε_F [23]. This energy cutoff is needed to avoid the divergence of the gap equation with the zero-range pairing force characterizing the BSk27 interaction [40,41]. The pairing strength is consistently estimated from Eq. (27) adopting the energy cutoff used in the BCS equations [Eqs. (13) and (14)].

The resulting pairing gaps $\Delta_q(\beta, \varepsilon)$ for a deformation β and an excitation energy ε are found to be lower than those obtained with the five-points approximation [Eq. (15)]. The corresponding states densities with lower pairing gaps are consequently larger leading to a fragmentation dominated by a heavy fragment in the vicinity of the doubly magic nucleus $^{50}_{132}\text{Sn}_{82}$, especially in ^{236}U and ^{240}Pu cases. The corresponding yields are shown in Fig. 9 (cyan lines) and compared those obtained by the SPY2 version (red lines) where the pairing gaps are deduced from the five-points mass difference [Eq. (15)]. Yields calculated using the five-points mass difference are seen to be in better agreement with experimental data than those calculated with the pairing energy. For this reason, we have adopted the five-points mass difference for the reference version of SPY2.

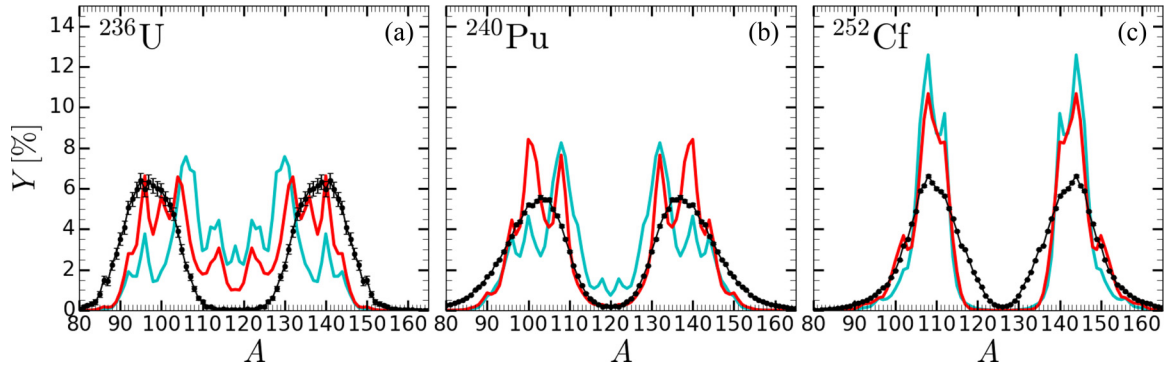


FIG. 9. On the left panels, the black dotted lines represent experimental (pre-neutron-emission) fission yields for fission of ^{236}U ($Q = 6.5$ MeV) (a) [34], ^{240}Pu ($Q = 6.5$ MeV) (b) [35], and fission of ^{252}Cf ($Q = 0$ MeV) (c) [36]. The cyan lines are smooth yields from SPY2 where Δ_q^0 is deduced from the pairing energy E_p^0 . The red lines are smooth yields both from SPY2 where Δ_q^0 is deduced from the five-points approximation.

C. Kinetic energy and diffuseness

The new definition of the scission point, based on the proton density at neck, links the KE to the fragments diffuseness which is linked to the external radius [Eq. (8)] and the effective one defined on the basis of the axial proton density [Eq. (7)],

$$d_{1/2} = R_{\text{ext}} - R_{\text{eff}} = a \ln \left(\frac{\rho_0}{0.5\rho_{\pi}^{\text{neck}}} - 1 \right). \quad (28)$$

We call $d_{1/2}$ half the diffuseness because it is defined in the same way as the diffuseness a and corresponds to the distance over which the axial proton density drops from $0.5\rho_0$ to ρ_{π}^{neck} . Since ρ_0 is rather insensitive to the deformation, $d_{1/2}$ varies similarly to the diffuseness a with respect to the deformation.

For the thermal neutron-induced fission of ^{239}Pu (Fig. 10), $d_{1/2}$ decreases with increasing fragment nucleon numbers. The lighter the fragments the larger the diffuseness. The

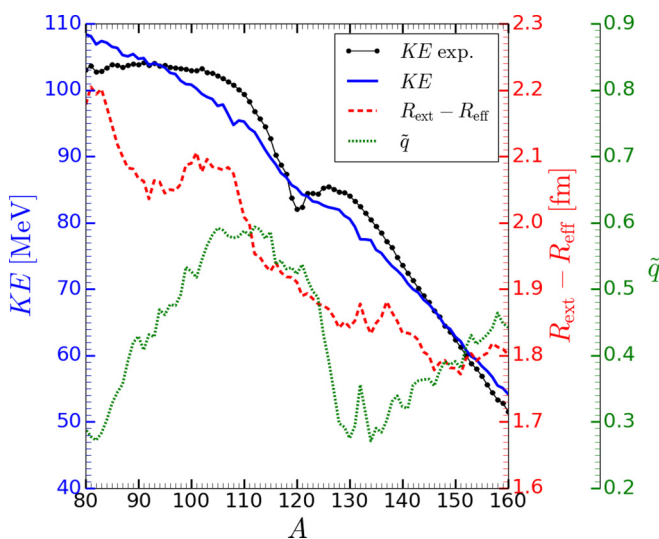


FIG. 10. KE distribution of fission of ^{240}Pu ($Q = 6.5$ MeV), from SPY2 model (blue curve) and from experimental (black curve) [38]. The half the diffuseness $d_{1/2} = R_{\text{ext}} - R_{\text{eff}}$ (red dashed line) and mean deformation \bar{q} (green dotted line).

dependence of $d_{1/2}$ with the fragment nucleon number differs significantly from the one ruling the mean fragment deformation \bar{q} because $d_{1/2}$ evolves in a nontrivial way with the nuclear deformation.

The local increase of half the diffuseness $d_{1/2}$ around $A = 100$ –110 and the complementary fragments $A = 130$ –140 explains the underestimate of the KE (Fig. 10). A complementary study using evaporated neutron distribution seems to indicate that the heavy $A = 130$ –140 fragments are too deformed, but it remains difficult to identify which fragments cause the underestimate of the KE.

D. TKE, fission yields and proton density at the scission neck

The impact on yields and kinetic energies are presented for the three fissioning systems for large variations of the proton density at the scission-neck from -50% to $+200\%$, Fig. 11. For the highest values of the density, the Blocki proximity potential and the more precise Reid-M3Y effective NN interaction are tested. The global trend of the yields [Figs. 11(a)–11(c)] are unaffected (at least for high fissility nuclei) by this variations showing that they are rather insensitive to the adopted value of the critical neck density, hence of the scission criterion. The KE distributions [Figs. 11(d)–11(f)] are more impacted by the change of the neck density since it directly affects the distance between the two fission fragments hence the coulomb repulsion between them. At high neck density, the KE of fragmentations around ($A_H = 132$, $A_L = A_{\text{CN}} - 132$) increases relatively more than the others. Their deformation at scission [Figs. 11(g)–11(i)] are also affected, the increase of the density implying a larger sensitivity to spherical shell effects.

The mean TKE of actinides follows a linear evolution with their fissility parameter [42], modeled by the Viola formula (Fig. 12). SPY1 and SPY2 propose a similar regular evolution. The shift between the distributions is simply due to the evolution of the distance between the two nascent fragments with the different criteria and has no special meaning. More interesting is the sensitivity to the role of the doubly magic nucleus ^{132}Sn for low-fissility nuclei with a high-density criteria at the neck. This doubly magic nucleus is responsible for the

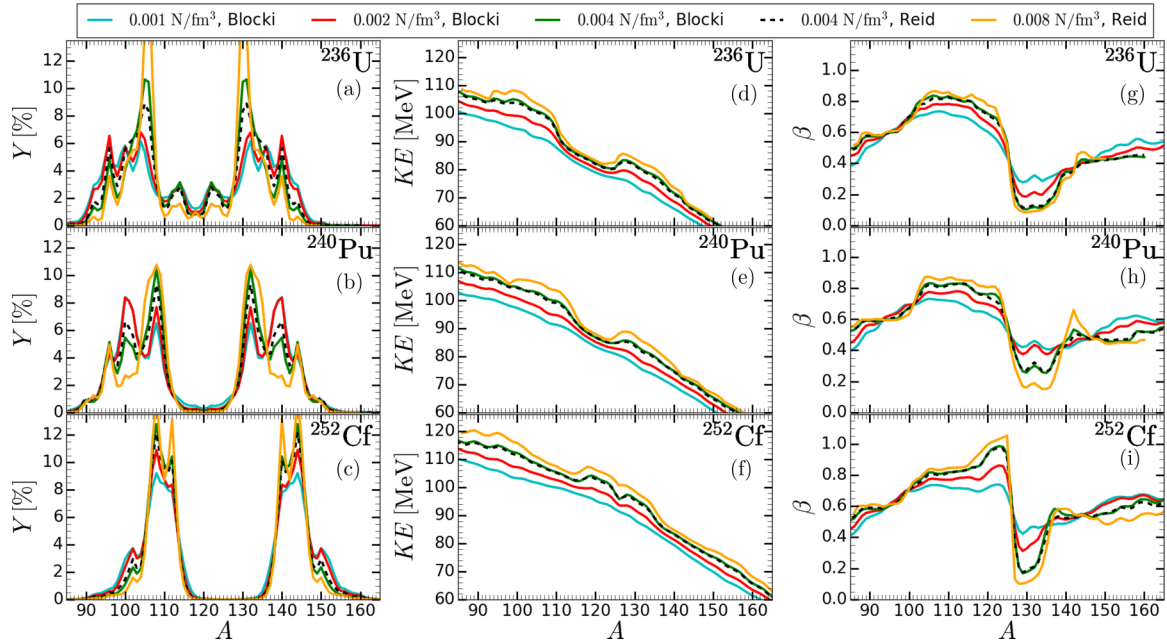


FIG. 11. Left panels (a–c), SPY2 smoothed yields for various neck densities for three fissioning systems. Central panels (d–f), corresponding SPY2 KE distributions. Right panels (g–i), corresponding mean deformations. Calculations are performed with $\rho_{\pi}^{\text{neck}} = 0.001 \text{ fm}^{-3}$ (cyan solid lines), $\rho_{\pi}^{\text{neck}} = 0.002 \text{ fm}^{-3}$ (red solid lines), $\rho_{\pi}^{\text{neck}} = 0.004 \text{ fm}^{-3}$ (green solid lines), and $\rho_{\pi}^{\text{neck}} = 0.008 \text{ fm}^{-3}$ (orange solid lines). The nuclear interaction energy between fragments is computed using the Blocki proximity potential [24], denoted by “Blocki” or alternatively in the $\rho_{\pi}^{\text{neck}} = 0.004$ and 0.008 fm^{-3} cases, numerically using the HFB nucleon distributions and the Reid-M3Y effective nucleon-nucleon interaction [25], denoted by “Reid” (back dashed curve).

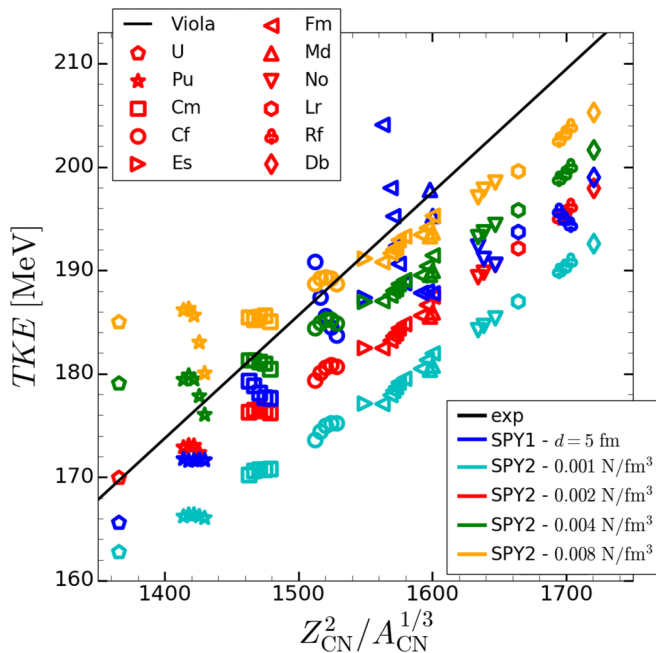


FIG. 12. Mean TKE as a function of the compound nucleus fissility parameter predicted by SPY with $Q = 8 \text{ MeV}$ and Viola formula [42] (black line). Data from SPY2 with $\rho_{\pi}^{\text{neck}} = 0.001 \text{ fm}^{-3}$ are in cyan, with $\rho_{\pi}^{\text{neck}} = 0.002 \text{ fm}^{-3}$ are in red, with $\rho_{\pi}^{\text{neck}} = 0.004 \text{ fm}^{-3}$ in green, and with $\rho_{\pi}^{\text{neck}} = 0.008 \text{ fm}^{-3}$ are in orange. Data from SPY1 are in blue.

asymmetric-symmetric transition zone $N_{\text{CN}} = 140$ of the low-fissility nuclei, as discussed in Sec. V A and in particular in Fig. 16(a). No precission kinetic energy is included yet in the model. Such contribution, varying from 0 MeV [43], 10 MeV [22,44], up to 20 MeV [45], depending on the model, could fill the gap between our actual description and the observed experimental trend. This contribution will be included as soon as we have access to a controlled description of it.

E. Sensitivity to the excitation energy

The excitation energy of the fissioning system clearly affects the energy balance and is theoretically taken into account in the E_{CN} term of Eq. (1). It can be written as $E_{\text{CN}} = M_{\text{CN}} + Q$, where M_{CN} is the mass of the fissioning system and Q its excitation energy. Note that only the first chance fission is taken into account in the SPY model and that individual binding energies and single-particle level schemes are calculated at zero temperature. For spontaneous fission, $Q = 0 \text{ MeV}$, while for thermal neutron-induced fission it corresponds to the neutron separation energy, i.e., for both ^{239}Pu and ^{235}U , $Q = 6.5 \text{ MeV}$. The symmetric part of the fission yields distribution is known to increase with increasing excitation energy of the fissioning system [12] and at very high excitation energies (several tens of MeV), the fission becomes essentially symmetric with the fissioning system behaving as a liquid drop. For the fission of actinides, such behavior is not yet reached with 14 MeV neutron-induced fission, the symmetric part of

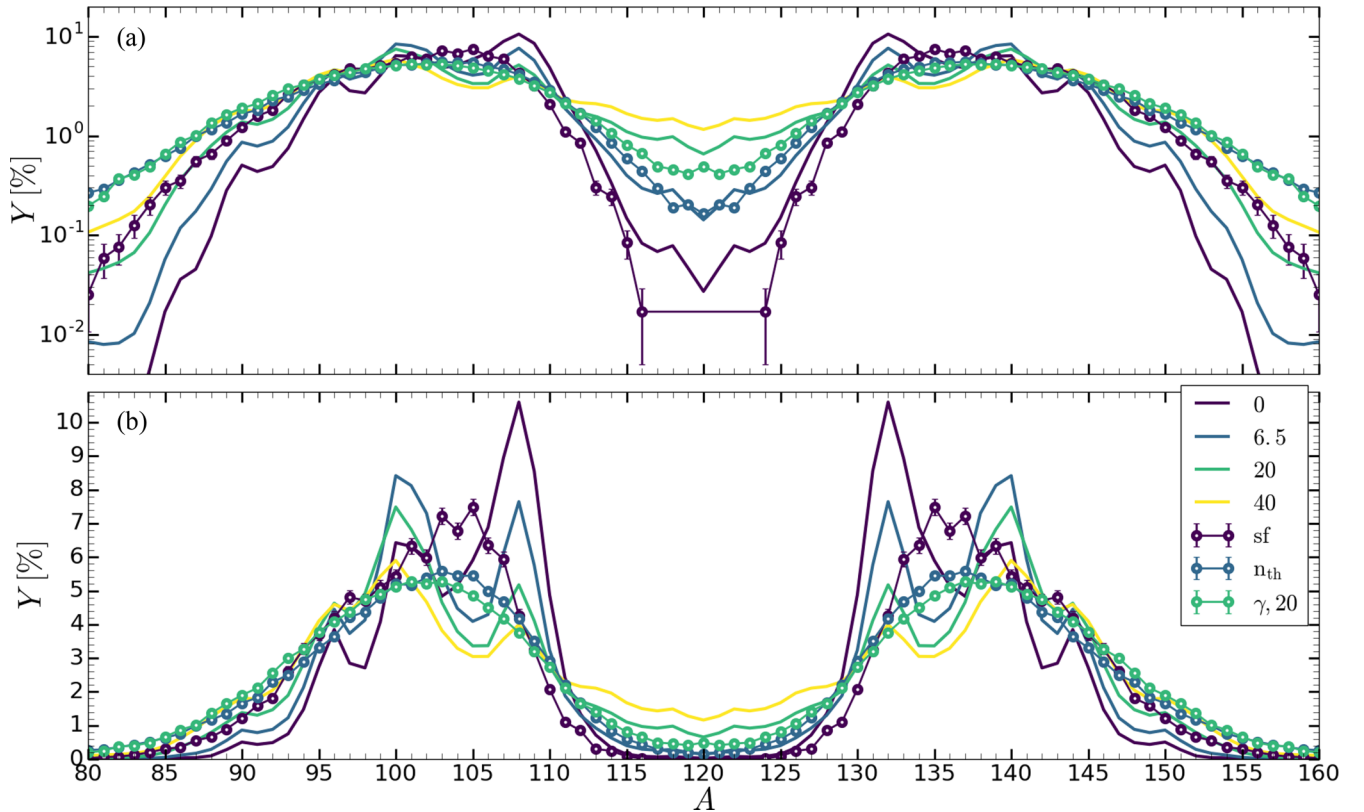


FIG. 13. SPY2 pre-neutron-emission smooth fission yields of ^{240}Pu as a function of the fragment mass number A for different initial excitation energies (in MeV), in log scale (a) and in linear scale (b). The excitation energy of 6.5 MeV corresponds to the thermal neutron-induced fission of ^{239}Pu . Solid lines with dots denoted by “sf” correspond to experimental data for spontaneous fission of ^{240}Pu [46], “nth” to the thermal neutron-induced fission of ^{239}Pu [35], and “ γ , 20” to the ^{240}Pu photofission with 20 MeV γ 's [47].

the isobaric fission yields increasing from about 0.01% to 1%. This feature is also observed for ^{240}Pu fission [Fig. 13(a), thin lines with dots] between the spontaneous fission [46] and the 20 MeV photofission [47]. SPY reproduces fairly well this feature compared to experimental data [Fig. 13(a), solid lines].

Another feature observed in experimental data is the shift of the most probable fragmentation towards more asymmetric fission with increasing excitation energy and, to a lesser extent, a shift of the mean value of the heavy peak [Fig. 13(b)]. Both features are also described by the SPY model. For the 0, 6.5 and 20 MeV energies, the mean value of the heavy peak amounts to 138.86, 139.38, and 139.2, respectively, for experimental data and 136.19, 137.46, and 137.87 for SPY. Concerning the most probable fragmentation, experimentally they are found at (105 + 135), (103 + 137), and (101 + 139), respectively, and with SPY at (108 + 132) and (100 + 140) in the two other cases. This rapid shift in SPY2 yields of the most probable fragmentation with excitation energy is due to the strong odd-even effect in the yields distribution.

In the framework of the SPY model, the increase of the symmetric contribution to the yields distribution with increasing energies can be understood in terms of available energy and number of available states. On the one hand, the initial excitation energy shifts the available energy of all fragmentations by a constant value, which consequently decreases the relative available energy differences between the fragments.

Since yields in a first approximation are proportional to the available energy, they will be less affected by these differences at high energy. On the other hand, at increasing energies, shell effects are washed out and the state densities becomes a simple Fermi gas relatively insensitive to the nuclear deformation. At high excitation energy, the fission system behaves as a liquid drop for which shell effects become negligible and stop affecting the yields distribution, hence favoring a symmetric fission.

F. Odd-even effects in yields

From the experimental point of view, the proton pairing effect in the isotopic yields is more accessible than the neutron one because the charge of a fragment is easily measurable [48,49]. The proton staggering in SPY2 isotopic yields is clearly too strong, but can be significantly reduced by applying our smoothing procedure [Eq. (26)], as illustrated in Fig. 14.

The isotopic yield staggering can be quantified by the proton odd-even effect amplitude δ_p [53],

$$\delta_p[\%] = \frac{\sum Y(Z_{\text{even}}) - \sum Y(Z_{\text{odd}})}{\sum Y(Z)}, \quad (29)$$

where $Y(Z)$ is the isotopic yields.

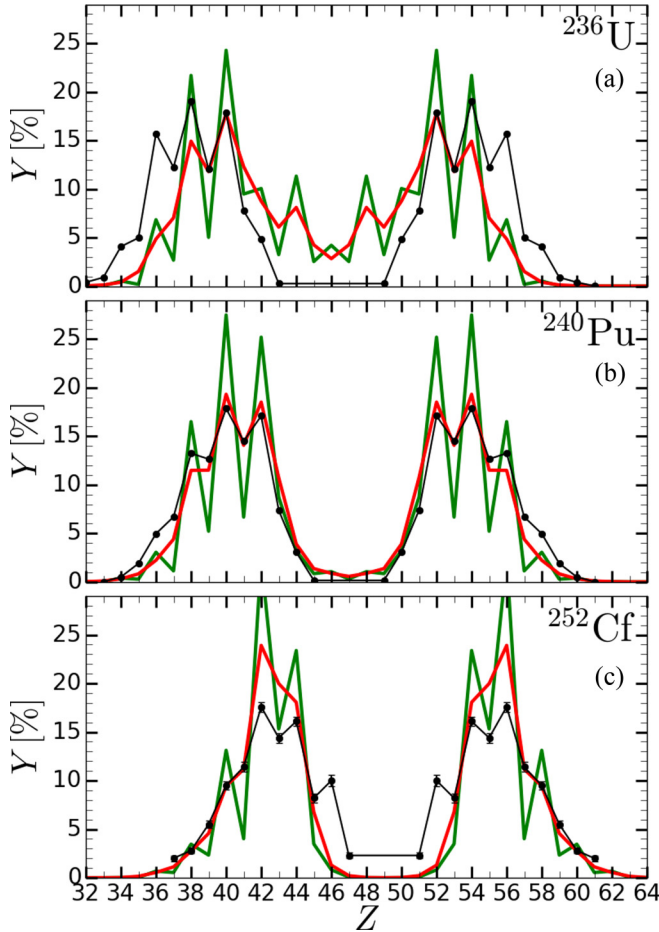


FIG. 14. The black dotted lines represent experimental isotopic fission yields for thermal neutron-induced fission of ^{235}U (a) [50], ^{239}Pu (b) [51], and the spontaneous fission of ^{252}Cf (c) [52]. The green lines are fission yields from SPY2, the red lines are smooth yields from SPY2.

Experimentally, the proton odd-even effect amplitude tends to decrease with increasing fissility parameter $Z_{\text{CN}}^2/A_{\text{CN}}^{1/3}$ [53], as given in Table I. The SPY2 results obtained with the raw and smooth yields are also given in Table I. The width $\sigma_{z,n}$ of the Gaussian function used to smooth raw yields [Eq. (26)] is chosen to reproduce at best the experimental proton odd-even effect in the Pu and Cf cases (see Fig. 14). Due to the large symmetric part of the U fission yields, the proton odd-even effect amplitude is however underestimated.

As mentioned in Sec. IV A, the pairing effect has an opposite impact on individual binding energies and state

TABLE I. Proton odd-even effect amplitude δ_p for isotopic yields on Fig. 14.

	$Z^2/A^{1/3}$	Exp. data	Raw	Smooth
^{235}U	1370	23.7	53.7	13.3
^{239}Pu	1422	13.4	53.8	13.4
^{252}Cf	1520	12.2	48.4	12.0

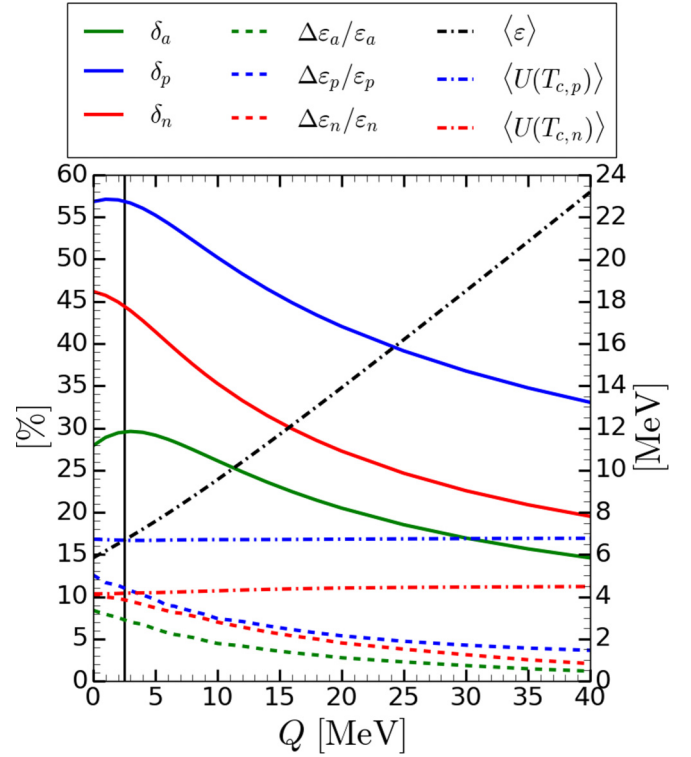


FIG. 15. Left y axis: nucleon (δ_a), neutron (δ_n), and proton (δ_p) odd-even effect amplitude derived from SPY2 raw isobaric, isotonic and isotopic fission yields, respectively, of ^{240}Pu as a function of the initial excitation energy Q (solid lines). Right y axis: excitation energy fluctuations $\Delta\varepsilon$ relative to the mean excitation energy of a fragment ε (dashed lines) and the mean excitation energy per fragment (ε), mean neutron and proton critical energies ($U(T_{c,q})$) (dot-dash lines). The vertical solid black line corresponds to the intersection between $\langle\varepsilon\rangle$ and $\langle U(T_{c,p})\rangle$ curves.

densities; consequently the strong pairing effect in the yields may be due to the low pairing effect in the state densities, in particular around the critical temperature. In the case of the neutron-induced fission of ^{239}Pu , the typical excitation energy of a fragment is around 7 MeV for the light fragment and 9 MeV for the heavy one which correspond generally to a temperature slightly higher than the critical temperature. For example, the proton critical temperature is reached at an excitation energy around 6 MeV for the open-shell nucleus ^{104}Mo . The low pairing effect in the state densities is due to the fast drop of the pairing gap to zero around the critical temperature. The pairing gap in a nucleus may however remain rather large for temperatures above the critical temperature when pairing gap fluctuations are taken into account [29]. For this reason, a way to increase the pairing effects in the state densities will be to introduce pairing gap fluctuations.

The odd-even staggering evolution is known to decrease with increasing excitation energies [12,53]. In the ^{240}Pu case, this trend is reproduced, as shown in Fig. 15. The neutron δ_n and nucleon δ_a odd-even effect amplitudes, defined in a way similar to the proton one Eq. (29), decrease as well. The

energy odd-even amplitudes

$$\frac{\Delta \varepsilon_q}{\varepsilon_q} = \frac{\sum \langle \varepsilon_q \rangle (X_{\text{even}}) - \sum \langle \varepsilon_q \rangle (X_{\text{odd}})}{\sum \langle \varepsilon_q \rangle (X)} \quad (30)$$

are also found to decrease with increasing initial excitation energies (Fig. 15).

The nucleon odd-even effect amplitude δ_a is lower than δ_p and δ_n ; this can be understood due to the small difference between the $\sum Y(A_{\text{even}})$ and $\sum Y(A_{\text{odd}})$ terms in Eq. (29). Indeed, in the former term, the fragmentations with two strongly paired fragments (even-even) are mixed with two weakly paired fragments (odd-odd), while in the latter the fragmentations with two moderately paired fragments (odd-even and even-odd) are mixed. The proton odd-even effect amplitude is higher than the neutron one, irrespective of the initial excitation energy, due to a narrower peak in the isotopic yields distribution compared to the isotonic one.

At low initial excitation energy, from $Q = 0$ up to around $Q = 2.5$ MeV, the proton and nucleon odd-even effect amplitudes are observed to increase slightly up to $Q = 2.5$ MeV, where the excitation energy of the fragments is higher than the proton critical energy (Fig. 15, vertical black line); at this energy, the proton pairing gap Δ_p cancels out. The increase of the proton and nucleon odd-even amplitudes is due to a decrease of the pairing effect in the state densities whereas the energy odd-even amplitudes do not decrease significantly at low Q .

For $Q > 2.5$ MeV, δ_p decreases due to the decrease of the energy odd-even amplitude, all significantly produced fragments having a zero proton and neutron pairing gap. Note that δ_n monotonically decreases because there is no neutron pairing effect in the state densities of the fragments, so that the excitation energy of the fragments from the spontaneous fission is above the neutron critical energy.

On the basis of statistical considerations using a canonical ensemble, Bocquet *et al.* [53] concluded that it was difficult to explain the evolution of the odd-even amplitude with excitation energies. SPY is based on a microcanonical ensemble and clearly predicts the decrease of odd-even effects with increasing initial energies in terms of available energy and number of available states. The energy odd-even amplitude becomes negligible at high energy and the state densities tend to a simple Fermi gas relatively insensitive to the nuclear deformation, leading to an attenuation of the odd-even staggering in the yields distribution. As a result, pairing no more impacts the fission yields.

The mean excitation energy of a fragment (ε) increases linearly with initial excitation energy Q from 5.8 to 23.2 MeV which represents an increase of 34.7 MeV of the total mean excitation energy for an increase of 40 MeV of the initial excitation energy. The increase of the initial excitation energy ends up mainly as excitation energy in fragments whereas the other part ends up as deformation energy which deforms the fragments and consequently decrease the KE.

V. SYSTEMATICS

SPY2 is now used to calculate systematically the fission yields for about 2000 heavy nuclei ranging between $Z = 78$

and $Z = 110$ (Fig. 16). Such a systematics allows us to study the impact of fragments shell effects on the fission mode [Fig. 16(a)], mean TKE [Fig. 16(c)], mean available energy [Fig. 16(e)], mean deformation of fragments [Fig. 16(d)], and mean number of evaporated neutrons [Fig. 16(f)]. The transitions between the fission modes are studied in details for the three representative isotopic chains of Pa, Cf, and Sg.

A. General discussion

Using the same peak analysis as in Ref. [5] for each isobaric yields distribution, it is possible to estimate the peak multiplicity corresponding to the number of significant humps characterizing the isobaric yields distribution. This analysis is performed with the raw fission yields distributions because it is not sensitive to the odd-even staggering. A multiplicity of one corresponds to a symmetric fission while a standard asymmetric fission is characterized by a multiplicity of two. For an isobaric yields distribution with three humps (i.e., for a peak multiplicity of three), the symmetric and an asymmetric fission are more or less equiprobable. We show in Fig. 16(a) the SPY2 peak multiplicity for all the 2000 nuclei with an initial excitation energy of 8 MeV. The SPY2 predictions can be compared to SPY1 [Fig. 16(b)], which found a peak multiplicity rather sensitive to the neutron number of the compound nucleus responsible for the vertical transitions seen in Fig. 16(b). This feature remains similar for SPY2 [Fig. 16(a)], though some local modifications are seen. In particular, less nuclei are depicted on the neutron-rich side in Fig. 16(a) in comparison with Fig. 16(b) because the fission of these nuclei is energetically forbidden in SPY2.

The fission of light nuclei $N_{\text{CN}} \leq 100$ is found to be always asymmetric; this is consistent with the asymmetric mode of ^{180}Hg [6,7]. The symmetric fission region with $100 < N_{\text{CN}} \leq 140$ is more extended with SPY2 than with SPY1 where the neutron-rich limit is obtained around $N_{\text{CN}} \approx 132$. According to experimental data [11], the transition from symmetric to asymmetric modes is located around $N_{\text{CN}} \approx 136$. The late transition predicted by the SPY2 model is responsible for the nonnegligible symmetric component found for $^{236}_{92}\text{U}_{144}$, as illustrated in Fig. 8(a). The transition between symmetric to asymmetric fission and the asymmetric fission mode of some nuclei are complex problems which have been extensively studied for the last decades, especially since the discovery of the mass asymmetry feature characterising the U fission [54–64]. It remains an open problem which has been mainly studied from different aspects, in particular considering the saddle or scission-points configuration of the fissioning system.

Between the symmetric and asymmetric regions, a triple-peak zone at $N_{\text{CN}} \approx 143$ and $84 < Z_{\text{CN}} < 94$ is found; this result is somewhat consistent with experimental observations, as inferred from the proton-induced fission of $^{226}_{88}\text{Ra}_{138}$ at an excitation energy of 18 MeV leading to a triple-hump yields distribution [12]. A similar triple-hump distribution is experimentally obtained for the high-energy neutron-induced fission of $^{232}_{90}\text{Th}_{142}$ at an excitation energy of 50–65 MeV [13]. The neutron-induced fission of $^{238}_{92}\text{U}_{146}$ is asymmetric at low energy and does not seem to transit through a triple-hump

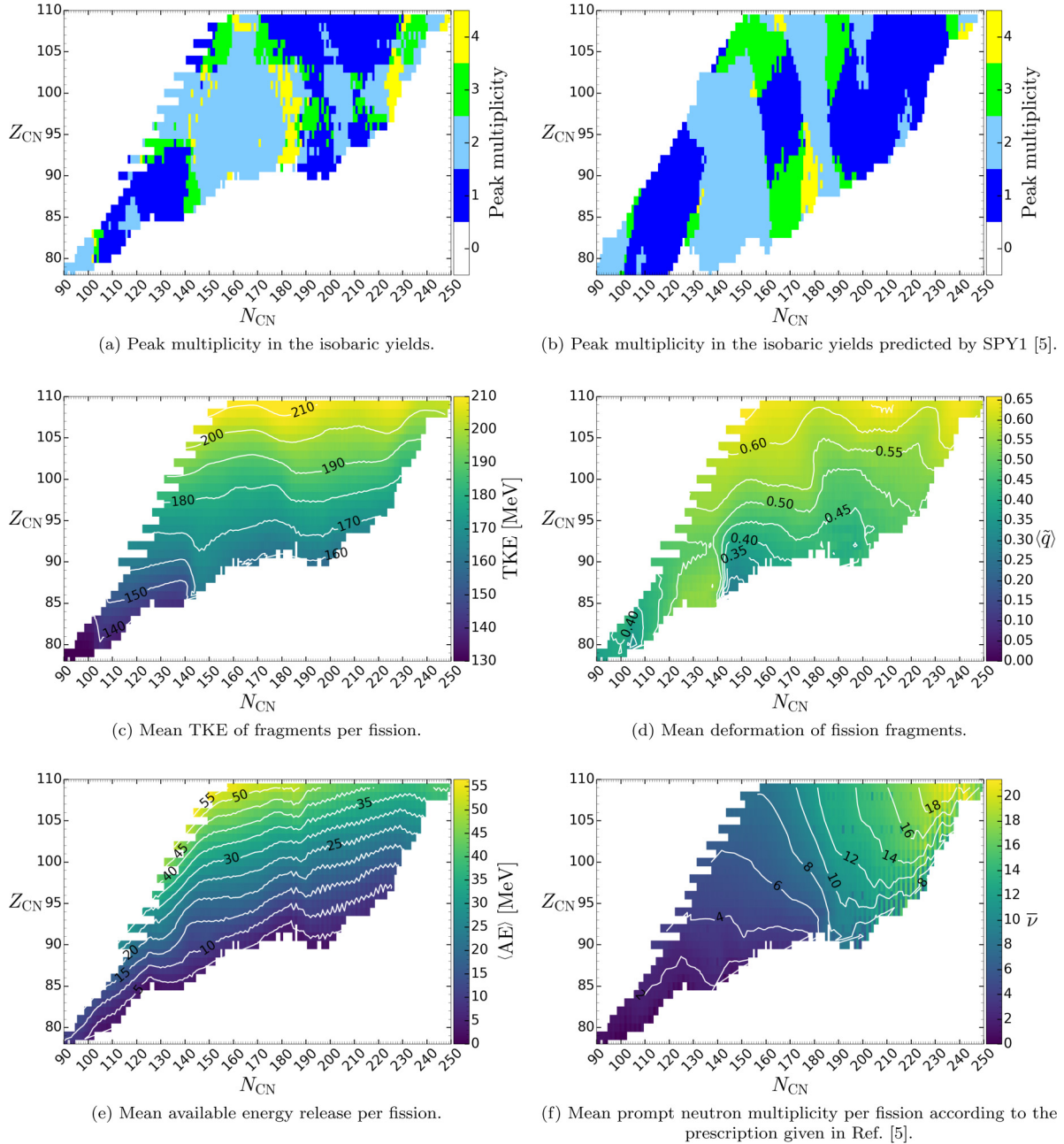


FIG. 16. Systematics in the (N, Z) plane of major fission observables for some 2000 nuclei between Pt and Mt for an initial excitation energy of $Q = 8$ MeV.

distribution before becoming symmetric at high excitation energy [13].

The symmetric $160 < N_{CN} < 170$ and $90 < Z_{CN} < 105$ regions predicted by SPY1 [Fig. 16(b)] disappears with SPY2. The doubly asymmetric fission zone shifts slightly from $N_{CN} \approx 178$ [Fig. 16(b)] to $N_{CN} \approx 184$ and is extended by SPY2 up to $Z_{CN} = 103$ [Fig. 16(a)]. These nuclei play a key role in explaining the origin of the rare-earth elements ($A \simeq 165$) during the r-process nucleosynthesis occurring in collapsing neutron stars [2]. Our new SPY2 version of the model confirms the conclusions of Ref. [2]. A new asymmetric region appears at $200 < N_{CN} < 222$ and $90 < Z_{CN} < 105$.

The explanation of these various transitions will be detailed in Sec. VB.

The mean TKE [Fig. 16(c)] increases mainly with the proton number of the fissioning system due to the Coulomb repulsion between fragments. If $Z_{CN} = Z_1 + Z_2$ (where Z_1 and Z_2 are the proton numbers of the first and second fragments) increases, then the TKE that can be expressed in a rough approximation as

$$\text{TKE [MeV]} = \frac{197}{137} \frac{Z_1 Z_2}{R_{\text{ext},1} + R_{\text{ext},2}} \quad (31)$$

also increases. The symmetric-to-asymmetric transition at $N_{\text{CN}} \approx 143$ is also visible in Fig. 16(c) with the sudden TKE increase. This result may appear as counterintuitive because symmetric splitting maximized the TKE according to Eq. (31). However, the deformation of the fragments cannot be neglected, and the TKE increase is caused by the decrease of the mean deformation of the fragments from $\bar{q} \approx 0.54$ to $\bar{q} \approx 0.32$ [see Fig. 16(d)]. Note that a drop of the mean deformation around $N_{\text{CN}} \approx 180$ can also be seen in Fig. 16(d) and can be associated with the four-peak zone.

The mean available energy [Fig. 16(e)] also increases with the neutron deficiency within a given isotopic chain and with the proton number of the fissioning nucleus. As a result, it increases roughly along the constant A_{CN} line. Around $N_{\text{CN}} = 126$ and 184, a drop of some MeV in the available energy is found. It can be explained by the neutron shell closure of the compound nucleus since a more bound fissioning nucleus release less energy. Note that all fissioning systems in Fig. 16 are computed with the initial excitation energy of $Q = 8$ MeV. Another drop is observed around $N_{\text{CN}} = 142$ and is associated with the transition between symmetric to asymmetric fission.

Finally, the mean number of evaporated neutrons [Fig. 16(f)] increases with the neutron number of the fissioning nucleus and is seen not to be significantly impacted by the fission mode. The more neutron rich the fissioning system, the more neutron rich the fragments, hence the larger the number of neutrons evaporated, especially for exotic neutron-rich nuclei for which the neutron separation energy is small.

B. Transition of fission modes

We show in Fig. 17 the isotonic fission yields and fragments deformation as a function of the neutron number of the fragment since the fission mode depends mainly on the neutron number of the fissioning nucleus [see Fig. 16(a)].

The Pa isotopic chain is representative of the transition between symmetric to asymmetric modes through a symmetric+asymmetric fission. This last fission mode occurs in the zone $140 < N_{\text{CN}} < 145$ for Pa [Fig. 17(a)]. In this zone, the heavy $N_{\text{frag}} \approx 82$ fragment becomes gradually spherical. When it is quasispherical with $\bar{q} < 0.1$, the fission mode is asymmetric whereas for $N_{\text{CN}} < 140$ the fission is symmetric and the fragments deformed with $\bar{q} > 0.2$ up to 0.4 for $N_{\text{CN}} = 125$ [Fig. 17(b)]. The asymmetric transition is associated with the appearance of the spherical $N = 82$ shell closure. Despite the offset in the transition from symmetric-to-asymmetric fission compared to experimental data, at $N_{\text{CN}} \approx 142$ instead of $N_{\text{CN}} \approx 136$ for thorium isotopic chain [11], the increase of the mean neutron number of the heavy peak, which depends on the neutron number of fissioning system, is in agreement with experimental data [11,65].

The fission becomes more and more asymmetric with increasing neutron number of the fissioning nucleus up to $N_{\text{CN}} = 180$. From $N_{\text{CN}} = 145$ to $N_{\text{CN}} = 180$, the light fragments are quite deformed, especially close to the symmetric fragmentation. The deformation of the heavy fragments are quasi-spherical for $N \approx 82$ which corresponds to the low asymmetric fragmentations, this deformation increases for heavier fragments. In a certain way, this feature is related to

the sawtooth shape of the evaporated neutron distribution per fragment. From $N_{\text{CN}} = 164$ up to $N_{\text{CN}} = 180$, the fragmentations close to the symmetric splitting with $N \approx 82$ are not spherical because the fragments with a neutron shell closure $N = 82$ are disfavored due to a low states density with respect to the deformed ones even if they release more energy. For these fragmentations, deformed fragments are preferred. In SPY1, where state densities did not include any shell effect, the fission used to be symmetric in this region due to the presence of the $N = 82$ shell closure in both fragments. But, in SPY2, the number of available states associated with this type of fragmentation is reduced which makes them less probable.

Between $N_{\text{CN}} = 180$ and $N_{\text{CN}} = 186$, fission is not energetically possible for an initial excitation energy $Q = 8$ MeV. For $N_{\text{CN}} > 186$, fission becomes again energetically possible and is symmetric because asymmetric fragmentations are not energetically reachable (less than 1 MeV) or beyond the neutron drip line. The spherical $N = 50$ shell closure is slightly visible but does not play a crucial role for the fission mode.

Cf isotopes fission asymmetrically up to $N_{\text{CN}} = 180$ [Fig. 17(c)]. The asymmetry increases with the increasing neutron number of the fissioning nucleus. For $N_{\text{CN}} \approx 146$, the $N = 82$ shell closure of the heavy fragment disfavors the fragmentation that includes this shell closure. The $N = 82$ shell closure disfavors also the spherical deformation of the fragments due to the low state density, except around $N_{\text{CN}} \approx 160$ where the $N = 82$ shell closure is present in both fragments of the fragmentations around the symmetric splitting [Fig. 17(d)]. Fragments are less deformed with respect to neighboring fissioning nuclei but they are not quasispherical. The neutron-deficient Cf isotopes give a fission close to a symmetric one because of the neutron shell closure in the fragments, $N = 50$ for the light one and $N = 82$ for the heavy one. For $180 < N_{\text{CN}} < 188$, a doubly asymmetric fission appears, the splitting of the asymmetric peaks being caused by the $N = 82$ shell closure of the light fragment. For neutron-rich Cf isotopes with $N_{\text{CN}} > 220$, the asymmetry splitting is limited by the $N = 126$ neutron shell closure of the heavy fragment.

The fission mode of Sg isotopes is mainly symmetric [Fig. 17(e)], except for the regions $150 < N_{\text{CN}} < 160$ and $170 < N_{\text{CN}} < 180$, where the distribution is triple humped, and the region $160 < N_{\text{CN}} < 170$, where the fission is asymmetric. The triple-hump fission and the asymmetric one are due to the presence of the spherical shell closure $N = 82$ in one of the two fragments. When this shell closure is in a fragment from a quasi-symmetric fragmentation (i.e., $N_{\text{CN}} \approx 164$), it disfavors them with respect to more asymmetric fragmentations. When this shell closure is in a fragment from an asymmetric fragmentation, it disfavors them with respect to symmetric fragmentation and more asymmetric ones which leads to a triple-peak fission. The three-peaks region with $230 < N_{\text{CN}} < 236$ and the asymmetric fission of $N_{\text{CN}} > 232$ result from the $N = 126$ shell closure of the heavy fragment which plays the same role as the shell closure $N = 82$ for lighter fissioning systems. The fragments deformation [Fig. 17(f)] is also slightly impacted by the $N = 82$ shell closure.

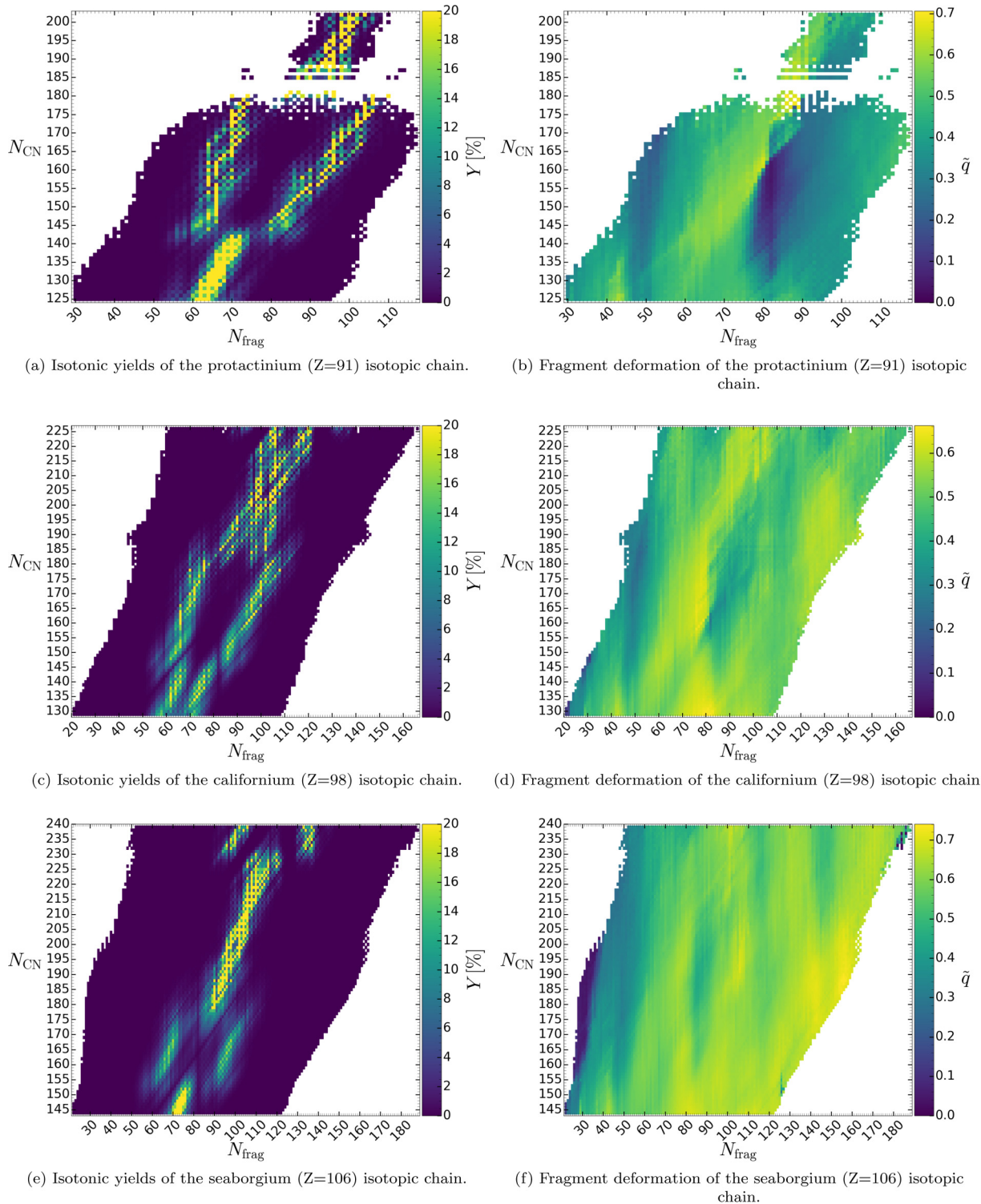


FIG. 17. Pre-neutron-emission isotonic yields on left panels of protactinium, californium and seaborgium isotopic chains with an excitation energy of $Q = 8$ MeV. These isotopic chains are representative of the evolution of the transition mode with the neutron number of compound nucleus in Fig. 16(a). On right panels, their corresponding mean deformation distribution.

VI. CONCLUSION

We presented an updated version of the scission-point model to estimate the yields as well as the KE distributions of the fragments resulting from the complex mechanism of

fission. In this updated SPY2 version, a new definition of the scission point is proposed. It is based on the mean-field proton density at the scission neck and assumes that the Coulomb repulsion between nascent fragments drives the evolution of the fissioning system between the saddle and scission points.

Moreover, HFB proton spatial distributions of the fragments are considered to compute the Coulomb repulsion energy between fragments. In contrast to our former version SPY1 [5], there is now no need to make assumptions on the proton distributions of the fragments. In addition, to calculate the phase space available to the fragments, we calculate the state densities now in a fully microscopic framework which takes pairing and shell effects coherently into account on the basis of the same nuclear structure properties, as the one used to estimate binding and Coulomb energies. All SPY2 inputs are computed within the same self-consistent microscopic HFB framework on the basis of the BSk27 Skyrme interaction.

In this updated SPY2 version, the fission yields calculation is significantly improved, in particular by predicting relatively wide peaks, as observed experimentally. The predicted KE distribution also better describes experiment. A detailed study was performed for the three fissioning systems for which measurements are available, namely ^{236}U , ^{240}Pu and ^{252}Cf . The KE distribution of ^{240}Pu has been analyzed on the basis of the deformation of the fragments and the scission distances. This study demonstrates that the assumption made in the SPY1 model concerning the constant scission distance was a rather good approximation. Without dynamical considerations, SPY2 is able to reproduce the evolution of fission yields distribution of ^{240}Pu with increasing excitation energies. The increase of the symmetric and largely asymmetric parts of the yields distribution is found to be in good agreement with experimental data.

Our systematic study of the fission mode for some 2000 heavy nuclei with $78 \leq Z \leq 110$ shows that the fission mode is mainly determined by the neutron number and that the TKE is correlated with the mean deformation of the fragments. The neutron shell closure of the fissioning nucleus also impacts the fragments distribution through the mean available energy, where the neutron shell closures of the fragments, in particular $N = 82$, plays a key role. The fragment deformation is less impacted by the neutron shell closures especially when a spherical shell closure strongly disfavors the spherical deformation due to the low state density of the fragments.

Although our new SPY model has proven its capacity to reproduce experimental data qualitatively well, for both the fission yields and KE distributions, further tests have to be performed with microscopic inputs computed with other nucleon-nucleon interactions. Further microscopical studies on the proton densities at scission neck will be performed to include some dependence with the proton and neutron number of the fissioning nucleus. The octupole degree of freedom also needs to be included for an extensive exploration of the available phase space. In particular, Scamps *et al.* [21] have shown that asymmetric fission of actinides can be induced by the octupole softness of open-shell nuclei rather than by the shell effect in closed shell nuclei. More work in this direction is foreseen. In addition, dynamical effects, such as friction or inertia, could improve the accuracy of the SPY model predictions by introducing a pre-scission kinetic energy that is missing in our purely static description.

ACKNOWLEDGMENT

This work has been supported by the Fonds De La Recherche Scientifique - FNRS (F.R.S-FNRS, Belgium).

APPENDIX A: COULOMB INTERACTION ENERGY BETWEEN TWO COAXIAL HOLLOW CYLINDERS

For fragments with a nonanalytical proton distribution, the Coulomb interaction energy has to be computed numerically. For two charged fragments of proton density distributions, $\rho_{\pi,i}(x_i, y_i, z_i)$, it is given by

$$E_{\text{coul}} = \sum_{i:\{x_1, y_1, z_1\}} \sum_{j:\{x_2, y_2, z_2\}} \frac{\rho_{\pi,i} \rho_{\pi,j} \Delta V_i \Delta V_j}{r_{ij}}, \quad (\text{A1})$$

$$r_{ij} = \sqrt{(x_2^2 - x_1^2)^2 + (y_2^2 - y_1^2)^2 + (z_2^2 - z_1^2)^2}.$$

The numerical calculations implies six nested loops which is computerwise time consuming. However, using the z -axisymmetric property of the proton density, the number of loops can be reduced to four. To achieve this, the Coulomb interaction energy between two coaxial hollow cylinders has to be determined analytically from the proton densities and their geometrical characteristics, i.e., radius, thickness and width (see Fig. 18).

The Coulomb interaction energy between two coaxial hollow cylinders $c1$ and $c2$ of proton densities $\rho_{\pi,1}$ and $\rho_{\pi,2}$, respectively, is given (in MeV) by

$$dE_{\text{coul}}^{c1c2} = \frac{197}{137} r_1 dr_1 r_2 dr_2 dz_1 dz_2 \rho_{\pi,1} \rho_{\pi,2} \times \underbrace{\int_0^{2\pi} \int_0^{2\pi} \frac{d\varphi_1 d\varphi_2}{\|\vec{r}_{12}\|}}_{f(r_1, r_2, d_{12})} \quad (\text{A2})$$

To obtain an analytical expression for dE_{coul}^{c1c2} , the function $f(r_1, r_2, d_{12})$ can be reduced to a one variable function times a factor where the variable and the factor depend on the cylinders radii and their respective distance. Let us define the

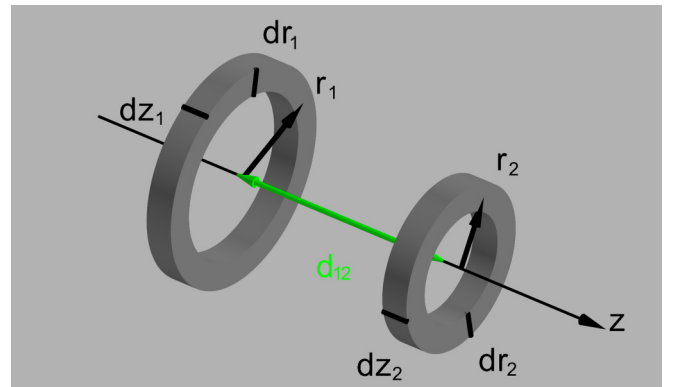


FIG. 18. Schematic representation of two coaxial hollow cylinders along the z axis. Each hollow cylinder is characterized by a width dz_i , a radius r_i and a thickness dr_i . The cylinders are distant by d_{12} .

vector \vec{r}_{12} as

$$\vec{r}_{12} = -r_1 \begin{pmatrix} \cos(\varphi_1) \\ \sin(\varphi_1) \\ 0 \end{pmatrix} + d_{12} \begin{pmatrix} 0 \\ 0 \\ 1 \end{pmatrix} + r_2 \begin{pmatrix} \cos(\varphi_2) \\ \sin(\varphi_2) \\ 0 \end{pmatrix}. \quad (\text{A3})$$

The squared norm of this vector is given by

$$\begin{aligned} r_{12}^2 &= \alpha^2 [1 - \beta \cos(\varphi_1 - \varphi_2)] \\ &= \alpha^2 (1 - \beta) \left[1 - \frac{2\beta}{\beta - 1} \sin^2 \left(\frac{\varphi_1 - \varphi_2}{2} \right) \right], \end{aligned} \quad (\text{A4})$$

where α and β are defined by

$$\alpha^2 = r_1^2 + d_{12}^2 + r_2^2, \quad (\text{A5})$$

$$\beta = \frac{2r_1 r_2}{\alpha^2} \quad (\text{A6})$$

and depend on the cylinders radii and their respective distance. The distance $\alpha\sqrt{1+\beta}$ corresponds to the longest distance between two points of the cylinders and $\alpha\sqrt{1-\beta}$ to the shortest one. The function $f(r_1, r_2, d_{12})$ can now be expressed as

$$f(r_1, r_2, d_{12}) = \frac{1}{\alpha\sqrt{1-\beta}} \underbrace{\int_0^{2\pi} \int_0^{2\pi} \frac{d\varphi_1 d\varphi_2}{\sqrt{1 - \frac{2\beta}{\beta-1} \sin^2 \left(\frac{\varphi_1 - \varphi_2}{2} \right)}}_{g(\beta)}, \quad (\text{A7})$$

where β varies from zero to one. The $\beta = 0$ case corresponds to the configuration where at least one of two hollow cylinders has a zero radius. The $\beta = 1$ case corresponds to a nonphysical case where both cylinders are confounded ($d_{12} = 0$ and $r_1 = r_2$). With a few changes of variables, $g(\beta)$ can be expressed in terms of an elliptic integral of the first kind K [66]:

$$g(\beta) = 8\pi K \left(-\sqrt{\frac{2\beta}{1-\beta}} \right), \quad (\text{A8})$$

where

$$K(k) = \int_0^{\pi/2} \frac{du}{\sqrt{1 - k^2 \sin^2(u)}}. \quad (\text{A9})$$

The $g(\beta)$ function can be interpreted as a dimensionless shape factor of the two hollow cylinders configuration. Even if this function is not analytical, it can be tabulated because β varies from zero to one. The Coulomb interaction energy between two coaxial hollow cylinders of width Δz , internal radius $r_i - \Delta r/2$, external radius $r_i + \Delta r/2$ separated by a distance d_{12} and a proton density $\rho_{\pi,i}$ can finally be obtained from

$$\begin{aligned} \Delta E_{\text{coul}}^{c1c2}(r_1, r_2, d_{12}) &= \frac{197}{137} r_1 \Delta r_1 r_2 \Delta r_2 \rho_{\pi,1} \rho_{\pi,2} (\Delta z)^2 \\ &\times \frac{1}{\alpha} \frac{1}{\sqrt{1-\beta}} 2\pi K \left(-\sqrt{\frac{2\beta}{1-\beta}} \right), \end{aligned} \quad (\text{A10})$$

where the Coulomb interaction energy is expressed in MeV, the lengths Δz , r_i , d_{12} in fm and the proton density in fm^{-3} .

APPENDIX B: NUCLEAR INTERACTION ENERGY BETWEEN TWO COAXIAL HOLLOW CYLINDERS

As for the Coulomb interaction energy between two fragments with a nonanalytical proton distribution (see Appendix A), the nuclear interaction energy has to be computed numerically. The Reid-M3Y effective nucleon-nucleon interaction [25,26],

$$v_{\text{eff}}(\rho, r_{12}) = g(r_{12})f(\rho), \quad (\text{B1})$$

$$g(r_{12}) = \sum_{k=1,2} \lambda_k \frac{e^{-b_k r_{12}}}{b_k r_{12}}, \quad (\text{B2})$$

$$f(\rho) = C(1 + \alpha e^{-\beta\rho}), \quad (\text{B3})$$

where ρ is the nucleon density, is used to compute nuclear interaction energy. This interaction is a product of a radial term and a density-dependent function [Eq. (B1)]. The radial term [Eq. (B2)] is energy-independent because this dependence is assumed to be of zero range with a sum of a short range (0.25 fm) repulsive term ($\lambda_1 = 7999 \text{ MeV}$ and $b_1 = 4 \text{ fm}^{-1}$) plus a medium range (0.4 fm) attractive term ($\lambda_2 = -2134 \text{ MeV}$ and $b_2 = 2.5 \text{ fm}^{-1}$). The density term [Eq. (B3)] depends on the sum of the density of each fragment: $\rho = \rho_1 + \rho_2$ separated by r_{12} , with $C = 0.44073$, $\alpha = 4.3259$, and $\beta = 10.639 \text{ fm}^3$.

The nuclear interaction energy between two coaxial hollow cylinders can be deduced in the same way as the Coulomb interaction energy, i.e.,

$$\begin{aligned} \Delta E_{\text{nuc}}^{c1c2}(r_1, r_2, d_{12}) &= r_1 \Delta r_1 r_2 \Delta r_2 \rho_{\text{nuc},1} \rho_{\text{nuc},2} (\Delta z)^2 \\ &\times f(\rho) \sum_{k=1,2} 8\pi \lambda_k \underbrace{\int_0^{\pi/2} \frac{e^{-R_k \sqrt{1 - \frac{2\beta}{\beta-1} \sin^2(u)}}}{R_k \sqrt{1 - \frac{2\beta}{\beta-1} \sin^2(u)}} du}_{\tilde{f}(\beta, R_k)}, \end{aligned} \quad (\text{B4})$$

with $R_k = b_k \alpha \sqrt{1-\beta}$, β is given by Eq. (A6), and $\rho_{\text{nuc},i}$ is the nucleon density of the fragment i . Like the function $g(\beta)$ [Eq. (A8)], $\tilde{f}(\beta, R_k)$ is not an analytical function but can be tabulated because β varies from zero to one and $R_k \in [0, 16]$. Beyond a given distance between the two hollow cylinders, the nuclear interaction energy becomes negligible. The maximal shortest distance $\alpha\sqrt{1-\beta}$ is fixed at 4 fm to decrease significantly the computation time.

The $\tilde{f}(\beta, R_k)$ function can be considered as a shape factor of the two hollow cylinders configuration like the $g(\beta)$ shape factor in the Coulomb interaction case (see Appendix A).

- [1] M. Arnould, S. Goriely, and K. Takahashi, *Phys. Rep.* **450**, 97 (2007).
- [2] S. Goriely, J.-L. Sida, J.-F. Lemaître, S. Panebianco, N. Dubray, S. Hilaire, A. Bauswein, and H.-T. Janka, *Phys. Rev. Lett.* **111**, 242502 (2013).
- [3] O. Just, A. Bauswein, R. A. Pulpillo, S. Goriely, and H.-T. Janka, *Monthly Notices Roy. Astron. Soc.* **448**, 541 (2015).
- [4] S. Goriely, *Eur. Phys. J. A* **51**, 22 (2015).
- [5] J.-F. Lemaître, S. Panebianco, J.-L. Sida, S. Hilaire, and S. Heinrich, *Phys. Rev. C* **92**, 034617 (2015).
- [6] A. N. Andreyev, J. Elseviers, M. Huyse, P. Van Duppen, S. Antalic, A. Barzakh, N. Bree, T. E. Cocolios, V. F. Comas, J. Diriken, D. Fedorov, V. Fedosseev, S. Franchoo, J. A. Heredia, O. Ivanov, U. Köster, B. A. Marsh, K. Nishio, R. D. Page, N. Patronis, M. Seliverstov, I. Tsekhanovich, P. Van den Bergh, J. Van De Walle, M. Venhart, S. Vermote, M. Veselsky, C. Wagemans, T. Ichikawa, A. Iwamoto, P. Möller, and A. J. Sierk, *Phys. Rev. Lett.* **105**, 252502 (2010).
- [7] S. Panebianco, J.-L. Sida, H. Goutte, J.-F. Lemaître, N. Dubray, and S. Hilaire, *Phys. Rev. C* **86**, 064601 (2012).
- [8] N. Bohr and J. A. Wheeler, *Phys. Rev.* **56**, 426 (1939).
- [9] V. Denisov, T. Margitych, and I. Sedykh, *Nucl. Phys. A* **958**, 101 (2017).
- [10] L. Wilets, *Theories of Nuclear Fission*, Oxford library of the physical sciences (Clarendon Press, Oxford, 1964).
- [11] K.-H. Schmidt, S. Steinhäuser, C. Bockstiegel, A. Grewe, A. Heinz, A. Junghans, J. Benlliure, H.-G. Clerc, M. de Jong, J. Müller, M. Pfützner, and B. Voss, *Nucl. Phys. A* **665**, 221 (2000).
- [12] C. Wagemans, *The Nuclear Fission Process* (Taylor & Francis, London, 1991), Chap. 8.
- [13] I. V. Ryzhov, S. G. Yavshits, G. A. Tutin, N. V. Kovalev, A. V. Saulski, N. A. Kudryashev, M. S. Onegin, L. A. Vaishnene, Y. A. Gavrikov, O. T. Grudzevich, V. D. Simutkin, S. Pomp, J. Blomgren, M. Österlund, P. Andersson, R. Bevilacqua, J. P. Meulders, and R. Prieels, *Phys. Rev. C* **83**, 054603 (2011).
- [14] C. Zöllner, A. Gavron, J. Lestone, M. Mutterer, J. Theobald, A. Iljinov, and M. Mebel, *Fission Fragment Properties in the $^{238}\text{U}(n,f)$ Reaction at Incident Neutron Energies from 1 MeV to 500 MeV* (World Scientific, Singapore, 1995) p. 56.
- [15] U. Brosa, H.-H. Knitter, T.-s. Fan, J.-m. Hu, and S.-I. Bao, *Phys. Rev. C* **59**, 767 (1999).
- [16] K.-H. Schmidt, B. Jurado, C. Amouroux, and C. Schmitt, *Nucl. Data Sheets* **131**, 107 (2016), special Issue on Nuclear Reaction Data.
- [17] H. Goutte, J. F. Berger, P. Casoli, and D. Gogny, *Phys. Rev. C* **71**, 024316 (2005).
- [18] N. Dubray, H. Goutte, and J.-P. Delaroche, *Phys. Rev. C* **77**, 014310 (2008).
- [19] C. Simenel and A. S. Umar, *Phys. Rev. C* **89**, 031601(R) (2014).
- [20] D. Regnier, N. Dubray, N. Schunck, and M. Verrière, *Phys. Rev. C* **93**, 054611 (2016).
- [21] G. Scamps and C. Simenel, *Nature* **564**, 382 (2018).
- [22] B. D. Wilkins, E. P. Steinberg, and R. R. Chasman, *Phys. Rev. C* **14**, 1832 (1976).
- [23] S. Goriely, N. Chamel, and J. M. Pearson, *Phys. Rev. C* **88**, 061302(R) (2013).
- [24] J. Błocki, J. Randrup, W. Świątecki, and C. Tsang, *Ann. Phys.* **105**, 427 (1977).
- [25] A. Kobos, B. Brown, R. Lindsay, and G. Satchler, *Nucl. Phys. A* **425**, 205 (1984).
- [26] M. Brandan and G. Satchler, *Phys. Rep.* **285**, 143 (1997).
- [27] H. A. Bethe, *Phys. Rev.* **50**, 332 (1936).
- [28] P. Decowski, W. Grochulski, A. Marcinkowski, K. Siwek, and Z. Wilhelmi, *Nucl. Phys. A* **110**, 129 (1968).
- [29] L. Moretto, *Phys. Lett. B* **40**, 1 (1972).
- [30] L. Moretto, *Nucl. Phys. A* **185**, 145 (1972).
- [31] P. Demetriou and S. Goriely, *Nucl. Phys. A* **695**, 95 (2001).
- [32] D. Madland and J. Nix, *Nucl. Phys. A* **476**, 1 (1988).
- [33] R. Razavi, A. Behkami, and V. Dehghani, *Nucl. Phys. A* **930**, 57 (2014).
- [34] C. Romano, Y. Danon, R. Block, J. Thompson, E. Blain, and E. Bond, *Phys. Rev. C* **81**, 014607 (2010).
- [35] C. Tsuchiya, Y. Nakagome, H. Yamana, H. Moroyama, K. Nishio, I. Kanno, K. Shin, and I. Kimura, *J. Nucl. Sci. Technol.* **37**, 941 (2000).
- [36] S. Zeynalov, F.-J. Hamsch, and S. Oberstedt, *J. Korean Phys. Soc.* **59**, 1396 (2011).
- [37] H. Baba, T. Saito, N. Takahashi, A. Yokoyama, T. Miyauchi, S. Mori, D. Yano, T. Hakoda, K. Takamiya, K. Nakanishi, and Y. Nakagome, *J. Nucl. Sci. Technol.* **34**, 871 (1997).
- [38] K. Nishio, Y. Nakagome, I. Kanno, and I. Kimura, *J. Nucl. Sci. Technol.* **32**, 404 (1995).
- [39] F.-J. Hamsch and S. Oberstedt, *Nucl. Phys. A* **617**, 347 (1997).
- [40] E. Garrido, P. Sarriguren, E. Moya de Guerra, and P. Schuck, *Phys. Rev. C* **60**, 064312 (1999).
- [41] A. Bulgac and Y. Yu, *Phys. Rev. Lett.* **88**, 042504 (2002).
- [42] V. E. Viola, K. Kwiatkowski, and M. Walker, *Phys. Rev. C* **31**, 1550 (1985).
- [43] M. Borunov, P. Nadtoshy, and G. Adeev, *Nucl. Phys. A* **799**, 56 (2008).
- [44] U. Brosa, S. Grossmann, and A. Müller, *Phys. Rep.* **197**, 167 (1990).
- [45] L. Bonneau, P. Quentin, and I. N. Mikhailov, *Phys. Rev. C* **75**, 064313 (2007).
- [46] L. Demattè, C. Wagemans, R. Barthélémy, P. D’hondt, and A. Deruytter, *Nucl. Phys. A* **617**, 331 (1997).
- [47] H. Thierens, A. De Clercq, E. Jacobs, D. De Frenne, P. D’hondt, P. De Gelder, and A. J. Deruytter, *Phys. Rev. C* **23**, 2104 (1981).
- [48] W. Leo, *Techniques for Nuclear and Particle Physics Experiments: A How-to Approach* (Springer, Berlin, 1994).
- [49] G. Knoll, *Radiation Detection and Measurement* (John Wiley & Sons, New York, 2010).
- [50] W. Lang, H.-G. Clerc, H. Wohlfarth, H. Schrader, and K.-H. Schmidt, *Nucl. Phys. A* **345**, 34 (1980).
- [51] C. Schmitt, A. Guessou, J. Bocquet, H.-G. Clerc, R. Brissot, D. Engelhardt, H. Faust, F. Gönnerwein, M. Mutterer, H. Nifenecker, J. Pannicke, C. Ristori, and J. Theobald, *Nucl. Phys. A* **430**, 21 (1984).
- [52] G. Mariolopoulos, C. Hamelin, J. Blachot, J. Bocquet, R. Brissot, J. Crançon, H. Nifenecker, and C. Ristori, *Nucl. Phys. A* **361**, 213 (1981).
- [53] J. Bocquet and R. Brissot, *Nucl. Phys. A* **502**, 213 (1989).
- [54] H. W. Newson, *Phys. Rev.* **122**, 1224 (1961).
- [55] I. Kelson, *Phys. Rev. Lett.* **20**, 867 (1968).
- [56] A. Iwamoto, S. Yamaji, S. Suekane, and K. Harada, *Prog. Theor. Phys.* **55**, 115 (1976).
- [57] M. G. Itkis, V. N. Okolovich, and G. N. Smirenkin, *Nucl. Phys. A* **502**, 243 (1989).

- [58] F. Haddad and G. Royer, *J. Phys. G: Nucl. Part. Phys.* **21**, 1357 (1995).
- [59] M. Brack, S. M. Reimann, and M. Sieber, *Phys. Rev. Lett.* **79**, 1817 (1997).
- [60] K.-H. Schmidt, J. Benlliure, and A. Junghans, *Nucl. Phys. A* **693**, 169 (2001).
- [61] J. Randrup, P. Möller, and A. J. Sierk, *Phys. Rev. C* **84**, 034613 (2011).
- [62] T. Ichikawa, A. Iwamoto, P. Möller, and A. J. Sierk, *Phys. Rev. C* **86**, 024610 (2012).
- [63] H. Paşca, A. Andreev, G. Adamian, and N. Antonenko, *Phys. Lett. B* **760**, 800 (2016).
- [64] H. Paşca, A. Andreev, G. Adamian, and N. Antonenko, *Nucl. Phys. A* **969**, 226 (2018).
- [65] K.-H. Schmidt and B. Jurado, *Physics Procedia* **31**, 147 (2012).
- [66] M. Abramowitz and I. Stegun, *Handbook of Mathematical Functions*, 10th ed., Applied Mathematics Series (U.S. Department of Commerce, National Bureau of Standards, Washington, DC, 1972).